J. Fluid Mech. (2006), *vol.* 553, *pp.* 187–226.
doi:10.1017/S0022112006008731 Printed in the United Kingdom

Dynamic simulation of spheroid motion between two parallel plane walls in low-Reynolds-number Poiseuille flow

By MICHELLE E. STABEN, ALEXANDER Z. ZINCHENKO† AND ROBERT H. DAVIS†

Department of Chemical and Biological Engineering, University of Colorado, Boulder, CO 80309-0424, USA

(Received 7 June 2005 and in revised form 28 September 2005)

A novel boundary-integral algorithm is used to study the general, three-dimensional motion of neutrally buoyant prolate and oblate spheroids in a low-Reynolds-number Poiseuille flow between parallel plates. Adaptive meshing of the spheroid surface assists in obtaining accurate numerical results for particle–wall gaps as small as 1.3% of the spheroid's major axis. The resistance formulation and lubrication asymptotic forms are then used to obtain results for arbitrarily small particle–wall separations. Spheroids with their major axes shorter than the channel spacing experience oscillating motion when the spheroid's centre is initially located in or near the midplane of the channel. For both two-dimensional and three-dimensional oscillations, the period length decreases with an increase in the initial inclination of the spheroid's major axis with respect to the lower wall. These spheroids experience tumbling motions for centre locations further from the midplane of the channel, with a period length that decreases as the spheroid is located closer to a wall. The transition from two-dimensional oscillating motion to two-dimensional tumbling motion occurs for an initial centre location closer to a wall as the initial inclination of the major axis is increased. For these spheroids, the average translational velocity along the channel length for two-dimensional oscillating motion decreases for an increase in the initial inclination of the major axis, and the average translational velocity for two-dimensional tumbling motion decreases for a decrease in the initial centre location. A prolate spheroid with its major axis 50% longer than the channel spacing and confined to the (x_2, x_3)-plane (where x_2 is the primary flow direction and x_3 is normal to the walls) cannot experience two-dimensional tumbling; instead, the spheroid becomes wedged between the walls for initial centre locations near the midplane of the channel when the initial inclination of the large spheroid's major axis is steep, and experiences two-dimensional oscillations for initial centre locations near a wall. When this spheroid's major axis is not confined to the (x_2, x_3)-plane, it experiences three-dimensional oscillations for initial centre locations in or near the midplane of the channel, and three-dimensional tumbling for initial centre locations near a wall.

1. Introduction

Low-Reynolds-number particle transport has applications in a broad array of fields, from classical chemical engineering processes, such as sedimentation (Romero,

† Authors to whom correspondence should be addressed: alexander.zinchenko@colorado.edu; robert.davis@colorado.edu

Agarwala & Davis 1993), to more novel applications, such as microfluidics (Beebe, Mensing & Walker 2002). In many of these applications, the problem of interest is the motion of a particle in a confined space, such as a long-and-narrow duct, which frequently can be accurately modelled as a parallel-plate geometry. Often, the particles of interest are non-spherical, including ellipsoidal and rod-like biological cells studied in microfluidic devices (Li & Harrison 1997; Chen *et al.* 2004) and disk-like red blood cells travelling through vessels (Brenner & Bungay 1971; El-Kareh & Secomb 2000).

Initially, researchers focused on the simpler task of modelling the motion of spherical particles between parallel plates, and work prior to 1965 is reviewed by Happel & Brenner (1986). Ganatos, Pfeffer & Weinbaum (1980*a*) and Ganatos, Weinbaum & Pfeffer (1980*b*) studied the force and torque on a sphere in creeping flow between two plane walls for motion both perpendicular and parallel to the walls, with their results being limited to locations where the gap between either wall and the edge of the sphere is at least 10% of its radius. Ganatos, Weinbaum & Pfeffer (1982) then combined these results from the collocation method (Ganatos *et al.* 1980*a*, *b*) with the one-wall lubrication asymptotics of Goldman, Cox & Brenner (1967*a*, *b*) to handle smaller separations. More recent work for a sphere in a low-Reynolds-number Poiseuille flow between two parallel plates is provided by Staben, Zinchenko & Davis (2003). In that work, the Green's function for the domain between two plane walls is used in the boundary-integral formulation, which allows incorporation of the wall effects without discretizing the bounding walls and use of well-established iterative methods. Accurate results were obtained for very small sphere–wall separations of less than 1% of the particle radius. These results were combined with a resistance formulation incorporating near-field asymptotic formulae (Goldman *et al.* 1967*a*, *b*) to describe the motion of spheres for arbitrarily small particle–wall separations. Translational and rotational velocity results for spheres with diameters up to 95% of the wall spacing were obtained.

Limited studies of non-spherical particles have also been performed for a parallel-plate geometry. A boundary-collocation method was used by Yu (1993) to study the instantaneous configurations of spheroids between two parallel plates, but the formulation did not allow analysis of near-contact interaction of the spheroid and the walls. Pozrikidis (1994) used the boundary-integral method to obtain the force and torque for oblate spheroids translating or rotating in a quiescent fluid or held fixed in a Poiseuille or Couette flow in a Hele-Shaw cell. However, the methodology utilized by Pozrikidis is based on a special velocity dependence on the azimuthal angle for a body of revolution with its axis perpendicular to the walls, which reduced the three-dimensional problem to a two-dimensional problem. Staben *et al.* (2003) also present limited results for the translational and rotational velocities of prolate ellipsoids between parallel walls.

Near-contact expressions are necessary for simulations in which the particle of interest is comparable in size to the spacing between the walls or moves in close proximity to the wall(s). The one-wall asymptotic formulae of Goldman *et al.* (1967*a*, *b*), employed by both Ganatos *et al.* (1980*a*, *b*) and Staben *et al.* (2003), are for a sphere and a plane wall only. To extend these near-field analytical solutions to non-spherical particles, asymptotic lubrication formulae for hydrodynamic interactions of arbitrarily shaped particles were obtained by Cox (1974), who addressed some of the simpler types of relative motion of the two surfaces. Subsequently, Claeys & Brady (1989) developed a more general asymptotic methodology that allows full description of the singular behaviour of hydrodynamic forces and torques, including higher-order terms of the cases that Cox (1974) considered. Near-field asymptotic solutions provide

one of the key components of the methodology used to obtain the results presented in this work.

To analyse dynamic trajectories of an ellipsoidal particle, which can have lateral drift in a slit even in Stokes flow due to its non-spherical shape, the predicted translational and rotational velocities obtained at each timestep from the quasi-steady Stokes solutions are used to update the particle position and orientation at each timestep. Dynamic solutions for the two-dimensional analogue of an ellipsoid in a parallel-plate geometry, namely an elliptic cylinder, in a Poiseuille flow between two plane walls, and for a three-dimensional ellipsoid in a Poiseuille flow in a tube, were obtained by Sugihara-Seki (1993, 1996). The two-dimensional elliptic cylinder formulation (Sugihara-Seki 1993) only allows examination of an ellipsoid with its major axis aligned in the plane perpendicular to the flow direction. This formulation is an idealization of ellipsoid motion between two walls, especially since this two-dimensional model cannot adequately predict motion when an ellipsoid is close to one or both walls. In this near-contact configuration, the force distribution over the surface of the particle is highly dependent upon the particle geometry near the bounding wall(s), since the local curvature of the particle surface has a strong effect on the results obtained. Sugihara-Seki (1996) followed the work on the two-dimensional elliptic cylinder with a study of the motion of a three-dimensional ellipsoid in low-Reynolds-number Poiseuille tube flow. In that study, the particle's axis was confined to the centreplane of the tube. The finite-element mesh used in those calculations was too sparse to allow highly accurate calculations near the walls, and no lubrication formulation was used to overcome this limitation. Additionally, the computational expense of the finite-element method at every timestep limited the results to a few trajectories.

Our goal in this work is to develop an efficient dynamic algorithm for analysing arbitrary three-dimensional motions of non-spherical particles in low-Reynolds-number Poiseuille flow between two infinite parallel plates. Results for particle orientations, trajectories, and velocities are presented for three sizes of prolate spheroids, one with a major axis larger than the wall spacing, and one size of oblate spheroid, for many different initial configurations. To obtain results for arbitrarily small spacings from the wall(s), analytical formulae for the lubrication asymptotics are used in combination with the boundary-integral simulations to handle the singular portions of the resistance coefficients. This methodology is similar in spirit but much more complex than that employed in our previous work for a sphere (Staben *et al.* 2003). Comparison of our results with the classical solution of Jeffery (1922) for a spheroid in an unbounded linear flow field is also made.

2. Numerical method

2.1. *Boundary-integral formulation*

Consider a force-free and torque-free particle with an arbitrary surface S between two parallel plane walls (figure 1) at low Reynolds number in a planar Poiseuille velocity field $\boldsymbol{u}_\infty = 4x_3(1-x_3)\boldsymbol{e}_2$ far from the particle. Non-dimensionalization of the problem is performed using the channel height, H, and the unperturbed fluid velocity at the midplane of the channel, U_c, as characteristic length and velocity scales, respectively. The characteristic viscous stress, $\mu U_c/H$, is used to non-dimensionalize stress, where μ is the fluid viscosity. The right-handed Cartesian coordinate system (x_1, x_2, x_3) is chosen with the $x_3 = 0$ plane as the lower wall and the x_2-axis oriented along the undisturbed flow direction. For the spheroids studied in this work, $a = c$ and b is the

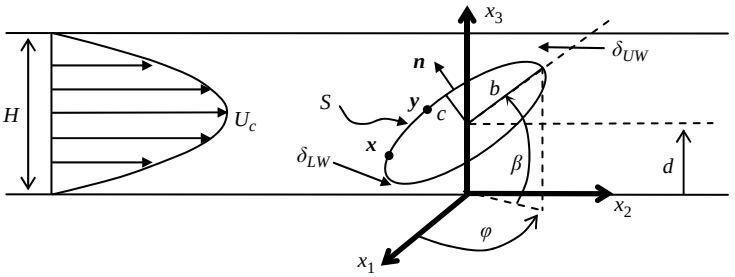

FIGURE 1. Problem geometry for spheroids at arbitrary angle and location with respect to the walls of the channel: d is the distance of the particle centre above the lower wall, U_c is the midplane Poiseuille fluid velocity, b is the unique half-axis (the major half-axis for a prolate spheroid, as shown, and the minor half-axis for an oblate spheroid), $a = c$ is the axisymmetric half-axis, β is the angle between the particle's axis of symmetry and the $x_3 = 0$ plane, and φ is the angle between the x_1-axis and the projection of the particle's axis of symmetry onto the $x_3 = 0$ plane. In boundary-integral calculations, $\boldsymbol{n}$ is the outward unit normal to the surface S at $\boldsymbol{x}$.

unique half-axis, which for prolate spheroids is the major half-axis and for oblate spheroids the minor half-axis. The instantaneous location of the particle centre is (x_1^c, x_2^c, x_3^c) with $x_3^c = d$ (the distance of the centre from the lower wall), β is the angle between the particle's axis of symmetry and the $x_3 = 0$ plane, and φ is the angle between the x_1-axis and the projection of the particle's axis of symmetry onto the $x_3 = 0$ plane (figure 1).

Our approach to formulating the deflated boundary-integral equation (e.g. Kim & Karilla 1991 and Pozrikidis 1992) is based on the Green's function $\boldsymbol{G}^k(\boldsymbol{x};\boldsymbol{y})$ and the corresponding pressure $\boldsymbol{p}^k(\boldsymbol{x};\boldsymbol{y})$ for the domain between two parallel plane walls. The vector field $\boldsymbol{G}^k(\boldsymbol{x};\boldsymbol{y}) = (G_1^k, G_2^k, G_3^k)$ is the Stokes flow velocity generated at $\boldsymbol{x}$ by the unit point force applied to the fluid at $\boldsymbol{y}$ in the direction of the kth Cartesian axis, and it satisfies the no-slip condition on the walls. Since the derivation has been described in detail previously (Staben *et al.* 2003), only the final deflated equation is presented here:

$$\psi_k(\boldsymbol{y}) = 2(u_\infty)_k(\boldsymbol{y}) - \psi'_k(\boldsymbol{y}) - 2\int_S \boldsymbol{\tau}_{\boldsymbol{n}}^k(\boldsymbol{x};\boldsymbol{y})\cdot\boldsymbol{\psi}(\boldsymbol{x})\,\mathrm{d}S_{\boldsymbol{x}} + \frac{n_k(\boldsymbol{y})}{S}\int_S \boldsymbol{\psi}(\boldsymbol{x})\cdot\boldsymbol{n}(\boldsymbol{x})\,\mathrm{d}S_{\boldsymbol{x}}, \qquad (2.1)$$

where $\boldsymbol{\tau}_{\boldsymbol{n}}^k = \tau_{ij}^k(\boldsymbol{x};\boldsymbol{y})n_j(\boldsymbol{x})\boldsymbol{e}_i$ is the stress vector for the fundamental solution, $\boldsymbol{\psi}(\boldsymbol{x})$ is a function to be determined, $\boldsymbol{\psi}'$ is the projection of $\boldsymbol{\psi}$ on the space of rigid-body motions, S is the surface area of the particle, and $\boldsymbol{n}(\boldsymbol{x})$ is the outward unit normal to S at $\boldsymbol{x}$. The right-hand-side operator of (2.1) has spectral radius less than unity (Kim & Karrila 1991; Pozrikidis 1992), allowing the unique solution $\boldsymbol{\psi}$ of (2.1) to be found by simple iterations. The particle translational velocity, $\boldsymbol{U}$, and rotational velocity, $\boldsymbol{\Omega}$, are found from

$$\boldsymbol{\psi}'(\boldsymbol{y}) = 2[\boldsymbol{U} + \boldsymbol{\Omega}\times(\boldsymbol{y} - \boldsymbol{x}^c)]. \qquad (2.2)$$

This formulation allows us in principle to determine the translational and rotational velocities of a particle in a low-Reynolds-number Poiseuille flow for any configuration of interest. However, repeated boundary-integral solutions of (2.1) at successive timesteps would take a prohibitively long computational time, especially for a particle in close proximity to the walls, because of the highly refined triangulations to describe lubrication and a large number of iterations needed in this case. An efficient alternative, allowing us to obtain accurate results for $\boldsymbol{U}$ and $\boldsymbol{\Omega}$ at arbitrarily small spacings, is to express them first in terms of resistance coefficients. For a particle with

velocities $\boldsymbol{U}$ and $\boldsymbol{\Omega}$ in a Poiseuille flow, the hydrodynamic forces and torques acting on the particle can be represented as

$$\mathscr{F} = \boldsymbol{R}\mathscr{U} + \mathscr{F}^p, \tag{2.3}$$

where $\mathscr{F} = (\boldsymbol{F}, \boldsymbol{T})$ is the force and torque vector, $\boldsymbol{R}$ is the resistance matrix for a particle in a quiescent fluid, $\mathscr{U} = (\boldsymbol{U}, \boldsymbol{\Omega})$ is the translational and rotational velocity vector, and $\mathscr{F}^p = (\boldsymbol{F}^p, \boldsymbol{T}^p)$ is the resistance vector for a particle rigidly held in a Poiseuille flow. For a force-free and torque-free particle in a Poiseuille flow, (2.3) reduces to $\mathscr{U} = -\boldsymbol{R}^{-1}\mathscr{F}^p$, where $\boldsymbol{R}^{-1} = \boldsymbol{M}$ is the mobility matrix. Poiseuille flow coefficients $\mathscr{F}^p$ do not contain singularities as the particle approaches a wall, and they can be pretabulated and accurately interpolated from a table in dynamic simulations. Singular lubrication contributions to resistance coefficients in $\boldsymbol{R}^{-1}$ are subtracted off, and the remaining smooth functions (referred to as Δ-coefficients) are pretabulated on a sufficiently fine mesh for dynamic simulations. In dynamic simulations, the Δ-coefficients are interpolated from the table and analytical lubrication contributions are added exactly to obtain accurate results for the resistance matrix $\boldsymbol{R}$.

To calculate $\boldsymbol{R}$ and $\mathscr{F}^p$, the boundary-integral formulation of (2.1) is generalized for the case of non-zero hydrodynamic force ($\boldsymbol{F}$) and torque ($\boldsymbol{T}$) acting on the particle to obtain

$$\psi_k(\boldsymbol{y}) = 2\left(-F_l G_l^k(\boldsymbol{x}^c;\boldsymbol{y}) - \frac{1}{2}\left.\frac{\partial \boldsymbol{G}^k}{\partial x_l}(\boldsymbol{x};\boldsymbol{y})\right|_{\boldsymbol{x}=\boldsymbol{x}^c} \cdot(\boldsymbol{T}\times\boldsymbol{e}_l) + (u_\infty)_k(\boldsymbol{y})\right) - \psi'_k(\boldsymbol{y}) - 2\int_S \boldsymbol{\tau}^k_{\boldsymbol{n}}(\boldsymbol{x};\boldsymbol{y})\cdot\boldsymbol{\psi}(\boldsymbol{x})\,\mathrm{d}S_{\boldsymbol{X}} + \frac{n_k(\boldsymbol{y})}{S}\int_S \boldsymbol{\psi}(\boldsymbol{x})\cdot\boldsymbol{n}(\boldsymbol{x})\,\mathrm{d}S_{\boldsymbol{X}}, \tag{2.4}$$

where $\boldsymbol{F}$ and $\boldsymbol{T}$ are the force and torque, respectively, acting on the particle; $\boldsymbol{x}^c = (x_1^c, x_2^c, x_3^c)$ is the particle's centre.

2.2. *Calculation of the boundary-integral operator*

Calculation of the fundamental stresslet found in (2.4) is based on detailed analyses of the Liron–Mochon (1976) explicit Fourier–Bessel integral representations of the Green's function and corresponding pressure, and allows us to represent them as (Staben *et al.* 2003)

$$\left.\begin{aligned} G_i^k(\boldsymbol{x};\boldsymbol{y}) &= \tilde{G}_i^k(\boldsymbol{x}-\boldsymbol{y}) + \left(G_i^k\right)_{LW}(\boldsymbol{x};\boldsymbol{y}) + \left(G_i^k\right)_{UW}(\boldsymbol{x};\boldsymbol{y}) + \hat{G}_i^k(\boldsymbol{x};\boldsymbol{y}),\\ p^k(\boldsymbol{x};\boldsymbol{y}) &= \tilde{p}^k(\boldsymbol{x}-\boldsymbol{y}) + (p^k)_{LW}(\boldsymbol{x};\boldsymbol{y}) + (p^k)_{UW}(\boldsymbol{x};\boldsymbol{y}) + \hat{p}^k(\boldsymbol{x};\boldsymbol{y}). \end{aligned}\right\} \tag{2.5}$$

The Green's function and pressure are separated into four terms: the free-space terms $\tilde{G}_i^k$ and $\tilde{p}^k$, lower-wall corrections $(G_i^k)_{LW}$ and $(p^k)_{LW}$, upper-wall corrections $(G_i^k)_{UW}$ and $(p^k)_{UW}$, and remaining non-singular functions $\hat{G}_i^k$ and $\hat{p}^k$, as shown in (2.5). The first three terms can be represented by analytical expressions that were derived by Lorentz (1896) and Blake (1971) and summarized by Pozrikidis (1992). The remaining functions $\hat{G}_i^k$ and $\hat{p}^k$ are not singular and are represented in terms of regularized Fourier–Bessel integrals (Appendix A of Staben *et al.* 2003). The regularized integrals are smooth functions of x_3, y_3 and $\rho^2 = (x_1 - y_1)^2 + (x_2 - y_2)^2$ up to the walls $x_3 = 0$, 1 and are pretabulated on a uniform mesh $x_3 = i/N$ ($-1 \leqslant i \leqslant N+1$), $y_3 = j/N$ ($0 \leqslant j \leqslant N$), and $\rho^2 = k\rho_{\max}^2/N_\rho$ ($0 \leqslant k \leqslant N_\rho + 1$), with typical parameters used being $N = 45$ and $N_\rho = 90$. The smooth nature of these functions allows extension of the mesh beyond the region of $0 \leqslant x_3 \leqslant 1$ for calculation of first-order and second-order derivatives by finite differences. The parameter $\rho_{\max}$ must not be smaller than the diameter of the particle-shape projection onto the $x_3 = 0$ plane;

in particular, $(\rho_{\max})^2 = 2.5$ sufficed for all calculations involving spheroidal particles with a dimensionless major axis length up to 1.5 times the channel height.

Standard singularity subtraction (e.g. Pozrikidis 1992) is used to eliminate the singular behaviour of the free-space part $\tilde{\boldsymbol{\tau}}$ of the fundamental stresslet (2.4) as $\boldsymbol{x} \to \boldsymbol{y}$. Near-singular behaviour of the wall-correction parts, $({}_{}\boldsymbol{\tau}^k_{\boldsymbol{n}})_{LW}$ and $({}_{}\boldsymbol{\tau}^k_{\boldsymbol{n}})_{UW}$, which occurs when $\boldsymbol{x} \approx \boldsymbol{y}$ and both points are close to the same wall, must also be eliminated by a near-singularity subtraction, as suggested by Staben *et al.* (2003). The expressions for the wall-correction integrands can be derived from Pozrikidis (1992) and are given by equation (19) of Staben *et al.* (2003). A significant acceleration of the code (by an order of magnitude) is achieved by representing the discrete form of the double-layer integrals as $\boldsymbol{N\Psi}$, where $\boldsymbol{\Psi}$ is an array of all $\boldsymbol{\psi}$-values in mesh nodes, and the matrix $\boldsymbol{N}$ is calculated before the iterations, which sets the limitation of $N_\triangle < 9000$, where $N_\triangle$ is the number of triangular boundary elements on S, for a PC with 1.5 GB of RAM. To accelerate the code even further, the biconjugate-gradient method of Lanczos (Fletcher 1976) is used instead of simple iterations for (2.4). Decisive advantage of using biconjugate-gradient iterations instead of simple iterations has been observed in other boundary-integral problems (Zinchenko, Rother & Davis 1997, 1999; Staben *et al.* 2003).

2.3. *Adaptive surface triangulations*

To mesh the surface of the particle, we start either from a regular icosaedron (Kim & Karrila 1991) or dodecaedron (Zinchenko *et al.* 1997) subject to a series of refinements to first obtain highly uniform triangulations of a unit sphere with $N_\triangle = 20 \times 4^k$ or 60×4^k ($k = 0,\ 1,\ 2, \ldots$) triangular elements. Each triangle face can be subdivided into m^2 smaller triangles (Loewenberg & Hinch 1996), which, when combined with the first two methods for small $m \leqslant 5$, gives additional possibilities $N_\triangle = 720$, 1500, 2160, 2880, 6000, 6480, etc., but still with highly uniform, unstructured-mesh triangulations for a unit sphere, the maximum-to-minimum mesh-edge ratio being within 1.19–1.22. This unit-sphere mesh is then stretched along the appropriate axes to obtain the desired spheroid mesh.

Gradual unstructured-mesh adaptation in near-contact areas for a sphere has been described in our previous work (Staben *et al.* 2003). A method similar in spirit but more complex in practice is used to perform the mesh adaptation for a spheroid. The initial non-uniform mesh described above is modified iteratively so that near-contact areas between the particle and the wall(s) have higher resolution, which greatly helps to reduce errors for these close-approach areas. The algorithm for moving the node points is

$$\boldsymbol{x}^{i,0}_{new} = \left(\sum_j w_j\right)^{-1} \sum_j w_j \boldsymbol{x}_j, \quad w_j = \frac{1}{h^\alpha_{LW}(\boldsymbol{x}_j)} + \frac{1}{h^\alpha_{UW}(\boldsymbol{x}_j)}, \tag{2.6}$$

where j refers to the neighbouring nodes $\boldsymbol{x}_j$ of node i, h_{LW} and h_{UW} are the distances of node j from the lower wall and upper wall, respectively, and $\alpha > 0$ is an adaptation parameter, where reasonable values for α were found not to exceed 0.5. To ensure gradual transition of the mesh, a relaxation parameter f is used, and a new position of node i is calculated as $\boldsymbol{x}^i_{new} = f\boldsymbol{x}^{i,0}_{new} + (1-f)\boldsymbol{x}^i$. The new position $\boldsymbol{x}^i_{new}$ is then moved radially along $\boldsymbol{x}^i_{new} - \boldsymbol{x}^c$ to return it to the particle surface:

$$(x_1', x_2', x_3') \to (\omega x_1', \omega x_2', \omega x_3'), \quad \omega = 1/\sqrt{(x_1'/a)^2 + (x_2'/b)^2 + (x_3'/c)^2}, \tag{2.7}$$

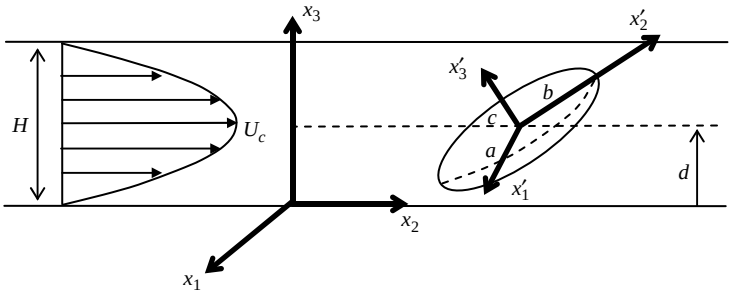

FIGURE 2. Problem geometry for the primed coordinate system, (x_1', x_2', x_3'), with the primed axes superimposed on a, b, c axes of the particle, shown with the fixed coordinate system defined in figure 1.

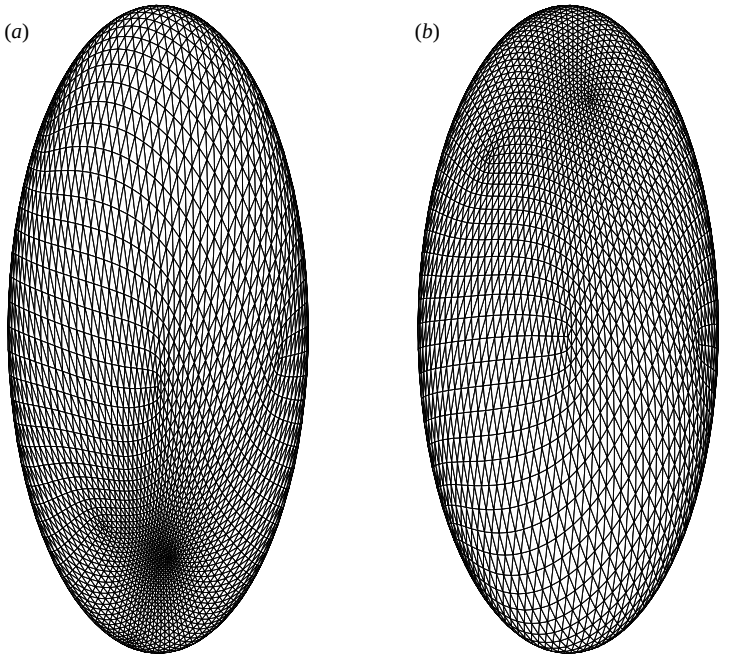

FIGURE 3. Sample mesh adaptation for prolate spheroid with $b/a = 2.5$, $2b/H = 1.5$ and $\beta/\pi = 0.186$ for $N_\triangle = 8640$ for (a) bottom view of the spheroid ($\delta_{LW}/H = 0.006$) and (b) top view of the spheroid ($\delta_{UW}/H = 0.026$).

where the primed coordinates refer to a Cartesian system centred on the spheroid and the axes of the coordinate system aligned with the spheroid axes, with x_1' along the a half-axis, x_2' along the b half-axis, and x_3' along the c half-axis (figure 2). A function χ is introduced,

$$\chi = \max_i(w_i \Delta x_i)/\min_i(w_i \Delta x_i), \tag{2.8}$$

where Δx_i is the minimum distance between node x_i and its neighbours. Iterations are performed until the function χ reaches a minimum. Mesh adaptivity near both walls is illustrated in figure 3 for a prolate spheroid with $b/a = 2.5$, $2b/H = 1.5$, $d/H = 0.49$, $\beta = 0.186\pi$ (33.5°) and $N_\triangle = 8640$, with the points of closest spacing of $0.006H$ and $0.026H$ from the lower wall and upper wall, respectively. Here, we achieve sufficient

adaptation so that, for the spacing shown in figure 3, the ratio of the maximum and minimum distances between neighbouring nodes is about 40. The mesh could be made more adaptive by increasing α, but we found that excessive adaptivity typically has a negative effect on the overall accuracy; $\alpha = 0.5$ was used in the calculations of § 3. A more general alternative that could be used is adaptive mesh restructuring in near-contact areas (Cristini, Blawzdziewicz & Loewenberg 2001), combined with mesh relaxations. However, we have found the relatively simple procedure described above to suffice for the present applications.

2.4. *Tabulation of resistance coefficients for dynamic simulation*

For a given centre location, d/H, and angle of inclination of the particle's axis of symmetry with respect to the channel walls, β, the boundary-integral formulation (2.4) is run (as described in §§ 2.1–2.3) to obtain the mobility coefficients, which are written to a mobility matrix $\boldsymbol{M}$ that is numerically inverted to obtain the resistance coefficient matrix $\boldsymbol{R} = \boldsymbol{M}^{-1}$. Singular portions are subtracted from the numerical values of the resistance coefficients using lubrication asymptotic formulae (to be discussed in § 2.5). The resulting differences (Δ-coefficients), along with Poiseuille flow coefficients $\mathscr{F}^p$ and other non-singular resistance coefficients, are tabulated for a range of β and d/H for each particle size and shape of interest.

For tabulation, it is convenient to describe $\boldsymbol{R}$ and $\mathscr{F}^p$ in a rotated coordinate system (x_1'', x_2'', x_2''), defined such that $x_3 = x_3''$, x_2'' is along the projection of the particle's axis of symmetry on the $x_3 = 0$ plane, and x_1'' is chosen to make (x_1'', x_x'', x_3'') a right-handed Cartesian coordinate system. The substantial advantage of using this coordinate system is that the hydrodynamic coefficients for a given particle size and shape are functions of β and d/H only. The variables described in the subsequent discussion (§§ 2.4–2.6) are assumed to be in this rotated coordinate system unless otherwise noted, although the double-prime notation has been omitted for clarity. In this rotated coordinate system, solution of the boundary-integral equations (2.4) is performed for eight individual cases: (i) unit hydrodynamic force $\boldsymbol{F} = \boldsymbol{e}_k$ acting on the particle along the kth coordinate axis with no imposed flow ($\boldsymbol{u}_\infty = \boldsymbol{T} = \boldsymbol{0}$, $k = 1, 2, 3$), (ii) unit torque $\boldsymbol{T} = \boldsymbol{e}_k$ acting on the particle about the kth coordinate axis with no imposed flow ($\boldsymbol{u}_\infty = \boldsymbol{F} = \boldsymbol{0}$, $k = 1, 2, 3$), and (iii) a force-free and torque-free particle in a Poiseuille flow along the x_1-axis or x_2-axis ($\boldsymbol{F} = \boldsymbol{T} = \boldsymbol{0}$, $\boldsymbol{u}_\infty = 4x_3(1 - x_3)\boldsymbol{e}_k$, $k = 1, 2$). Having solved for these eight individual cases, we can express $\boldsymbol{U}$ and $\boldsymbol{\Omega}$ for arbitrary $\boldsymbol{F}$ and $\boldsymbol{T}$ in a Poiseuille flow $\boldsymbol{u}_\infty = 4x_3(1 - x_3)(-\cos\varphi\ \boldsymbol{e}_1 + \sin\varphi \boldsymbol{e}_2)$ (where the term involving φ arises due to the coordinate system rotation), as $\mathscr{U} = \boldsymbol{M}\mathscr{F} + \mathscr{U}^p$, or in expanded form,

$$\begin{bmatrix} U_1 \\ U_2 \\ U_3 \\ \Omega_1 \\ \Omega_2 \\ \Omega_3 \end{bmatrix} = \begin{bmatrix} U_1^{F_1} & U_1^{F_2} & U_1^{F_3} & U_1^{T_1} & U_1^{T_2} & U_1^{T_3} \\ U_2^{F_1} & U_2^{F_2} & U_2^{F_3} & U_2^{T_1} & U_2^{T_2} & U_2^{T_3} \\ U_3^{F_1} & U_3^{F_2} & U_3^{F_3} & U_3^{T_1} & U_3^{T_2} & U_3^{T_3} \\ \Omega_1^{F_1} & \Omega_1^{F_2} & \Omega_1^{F_3} & \Omega_1^{T_1} & \Omega_1^{T_2} & \Omega_1^{T_3} \\ \Omega_2^{F_1} & \Omega_2^{F_2} & \Omega_2^{F_3} & \Omega_2^{T_1} & \Omega_2^{T_2} & \Omega_2^{T_3} \\ \Omega_3^{F_1} & \Omega_3^{F_2} & \Omega_3^{F_3} & \Omega_3^{T_1} & \Omega_3^{T_2} & \Omega_3^{T_3} \end{bmatrix} \begin{bmatrix} F_1 \\ F_2 \\ F_3 \\ T_1 \\ T_2 \\ T_3 \end{bmatrix} - \cos\varphi \begin{bmatrix} U_1^{p_1} \\ U_2^{p_1} \\ U_3^{p_1} \\ \Omega_1^{p_1} \\ \Omega_2^{p_1} \\ \Omega_3^{p_1} \end{bmatrix} + \sin\varphi \begin{bmatrix} U_1^{p_2} \\ U_2^{p_2} \\ U_3^{p_2} \\ \Omega_1^{p_2} \\ \Omega_2^{p_2} \\ \Omega_3^{p_2} \end{bmatrix}, \tag{2.9}$$

where U_i is the translational velocity in the ith direction, Ω_i is the rotational velocity about the ith axis, F_i is the hydrodynamic force imposed along the ith axis, T_i is the hydrodynamic torque imposed about the ith axis, and φ is defined with respect to the

fixed Cartesian system (figure 1). For the mobility matrix $\boldsymbol{M}$, the superscript refers to either force (F) or torque (T) (e.g. $U_3^{F_1}$ is the translational velocity along x_3 due to a force applied along x_1). For the Poiseuille flow coefficients $U_j^{p_i}$ and $\Omega_j^{p_i}$ in (2.9), the superscript p_i means Poiseuille flow along the ith axis. The 6×6 mobility matrix is numerically inverted to obtain the resistance matrix, $\boldsymbol{R} = \boldsymbol{M}^{-1}$, or

$$\begin{bmatrix} F_1^{t_1} & F_1^{t_2} & F_1^{t_3} & F_1^{r_1} & F_1^{r_2} & F_1^{r_3} \\ F_2^{t_1} & F_2^{t_2} & F_2^{t_3} & F_2^{r_1} & F_2^{r_2} & F_2^{r_3} \\ F_3^{t_1} & F_3^{t_2} & F_3^{t_3} & F_3^{r_1} & F_3^{r_2} & F_3^{r_3} \\ T_1^{t_1} & T_1^{t_2} & T_1^{t_3} & T_1^{r_1} & T_1^{r_2} & T_1^{r_3} \\ T_2^{t_1} & T_2^{t_2} & T_2^{t_3} & T_2^{r_1} & T_2^{r_2} & T_2^{r_2} \\ T_3^{t_1} & T_3^{t_2} & T_3^{t_3} & T_3^{r_1} & T_3^{r_2} & T_3^{r_3} \end{bmatrix} = \begin{bmatrix} U_1^{F_1} & U_1^{F_2} & U_1^{F_3} & U_1^{T_1} & U_1^{T_2} & U_1^{T_3} \\ U_2^{F_1} & U_2^{F_2} & U_2^{F_3} & U_2^{T_1} & U_2^{T_2} & U_2^{T_3} \\ U_3^{F_1} & U_3^{F_2} & U_3^{F_3} & U_3^{T_1} & U_3^{T_2} & U_3^{T_3} \\ \Omega_1^{F_1} & \Omega_1^{F_2} & \Omega_1^{F_3} & \Omega_1^{T_1} & \Omega_1^{T_2} & \Omega_1^{T_3} \\ \Omega_2^{F_1} & \Omega_2^{F_2} & \Omega_2^{F_3} & \Omega_2^{T_1} & \Omega_2^{T_2} & \Omega_2^{T_3} \\ \Omega_3^{F_1} & \Omega_3^{F_2} & \Omega_3^{F_3} & \Omega_3^{T_1} & \Omega_3^{T_2} & \Omega_3^{T_3} \end{bmatrix}^{-1}. \tag{2.10}$$

For the resistance coefficient matrix, F is force and T is torque, the subscript is the axis along which the force or around which the torque is exerted, and the superscript represents either translation along the ith axis (t_i) or rotation about the ith axis (r_i). For example, $F_1^{r_2}$ is the force along the x_1-axis due to rotation of the particle with unit angular velocity about x_2. Finally, the vector of resistance coefficients for a particle rigidly held in a Poiseuille flow is given by $\mathscr{F}^p = -\boldsymbol{R}\mathscr{U}^p$, as follows from (2.9) with $\mathscr{U} = \boldsymbol{0}$ and $\boldsymbol{R} = \boldsymbol{M}^{-1}$. The corresponding resistance formulation is then $\mathscr{F} = \boldsymbol{R}\mathscr{U} + \mathscr{F}^p$ in compact notation. Due to various symmetries in the problem that result from definition of the rotated coordinate system, many of the resistance coefficients in the 6×6 matrix of (2.10), as well as in the Poiseuille resistance coefficient vectors $\mathscr{F}^p$, are zero. For the most general case of a spheroid with its axes not aligned along any of the fixed coordinate system axes,

$$\begin{bmatrix} F_1 \\ F_2 \\ F_3 \\ G_1 \\ G_2 \\ G_3 \end{bmatrix} = \begin{bmatrix} F_1^{t_1} & 0 & 0 & 0 & F_1^{r_2} & F_1^{r_3} \\ 0 & F_2^{t_2} & F_2^{t_3} & F_2^{r_1} & 0 & 0 \\ 0 & F_3^{t_2} & F_3^{t_3} & F_3^{r_1} & 0 & 0 \\ 0 & T_1^{t_2} & T_1^{t_3} & T_1^{r_1} & 0 & 0 \\ T_2^{t_1} & 0 & 0 & 0 & T_2^{r_2} & T_2^{r_3} \\ T_3^{t_1} & 0 & 0 & 0 & T_3^{r_2} & T_3^{r_3} \end{bmatrix} \begin{bmatrix} U_1 \\ U_2 \\ U_3 \\ \Omega_1 \\ \Omega_2 \\ \Omega_3 \end{bmatrix} - \cos\varphi \begin{bmatrix} F_1^{p_1} \\ 0 \\ 0 \\ 0 \\ T_2^{p_1} \\ T_3^{p_1} \end{bmatrix} + \sin\varphi \begin{bmatrix} 0 \\ F_2^{p_2} \\ F_3^{p_2} \\ T_1^{p_2} \\ 0 \\ 0 \end{bmatrix}. \tag{2.11}$$

As a particle approaches a wall, the force needed to bring the surfaces together at a fixed approach velocity becomes infinite. To address this singular behaviour, analytical formulae for the lubrication contributions are subtracted from the numerical resistance coefficients to obtain Δ-coefficients, as described in the next section. In dynamic simulations (§ 2.6), these analytical lubrication contributions are added to the corresponding Δ-coefficients, allowing accurate description of the particle–wall interaction when the particle is in very close proximity to the bounding wall(s).

2.5. *Near-field asymptotic forms for an ellipsoid*

Of the 18 non-zero resistance coefficients in the 6×6 resistance matrix of (2.11), 13 are singular (all but $F_1^{r_3}$, $T_3^{t_1}$, $T_3^{r_2}$, $T_2^{r_3}$, and $T_3^{r_3}$). Near-field lubrication formulae for $F_2^{r_1}$, $T_1^{r_1}$, $F_1^{r_2}$, $T_2^{r_2}$, $F_1^{t_1}$, $T_2^{t_1}$, $F_2^{t_2}$, $T_1^{t_2}$, as well as the leading-order term of $F_3^{t_3}$, were obtained from Cox's (1974) solutions. In addition, we used the method of Claeys & Brady (1989) to derive the lubrication forms for the remaining coefficients $F_3^{r_1}$, $F_3^{t_2}$, $F_2^{t_3}$, and $T_1^{t_3}$. Lubrication contributions for each wall are additive, so these formulae can be

used for the particle–wall interaction with each wall. Essential details regarding the derivations can be found in Appendix A.

The 13 asymptotic formulae applicable to our problem are presented below (equations (2.12)–(2.16)), where the subscript o represents motion about a point o on the particle surface, which is the point of closest approach for the particle and a given wall; the hydrodynamic torques are assumed to be calculated about this point o. The subscript Cox refers to formulae obtained from Cox (1974), while the subscript CB is for the relations derived in Appendix A using the method of Claeys & Brady (1989).

Rotational motion about the x_1-axis:

$$\left(F^{r_1}_{2,Cox}\right)_o = -\frac{3\pi\ln(\delta)}{\sqrt{\lambda_1\lambda_2}}\left[\frac{1}{R_2\lambda_2(2\lambda_1+3\lambda_2)}-\frac{1}{2\lambda_1+3\lambda_2}\right], \tag{2.12a}$$

$$\left(F^{r_1}_{3,CB}\right)_o = -\frac{9}{4}\frac{\pi\ln(\delta)}{\sqrt{\lambda_1\lambda_2}(\lambda_1+\lambda_2)}\left[\frac{\kappa_1(2\lambda_1+\lambda_2)+\kappa_3(2\lambda_1+7\lambda_2)}{\sqrt{\lambda_2}(2\lambda_1+3\lambda_2)}\right], \tag{2.12b}$$

$$\left(T^{r_1}_{1,Cox}\right)_o = \frac{3\pi\ln(\delta)}{\sqrt{\lambda_1\lambda_2}}\left[\frac{1}{\lambda_2(2\lambda_1+3\lambda_2)}\right]. \tag{2.12c}$$

Rotational motion about the x_2-axis:

$$\left(F^{r_2}_{1,Cox}\right)_o = \frac{3\pi\ln(\delta)}{\sqrt{\lambda_1\lambda_2}}\left[\frac{1}{R_1\lambda_1(3\lambda_1+2\lambda_2)}-\frac{1}{3\lambda_1+2\lambda_2}\right], \tag{2.13a}$$

$$\left(T^{r_2}_{2,Cox}\right)_o = \frac{3\pi\ln(\delta)}{\sqrt{\lambda_1\lambda_2}}\left[\frac{1}{\lambda_1(3\lambda_1+2\lambda_2)}\right]. \tag{2.13b}$$

Lateral translation along the x_1-axis:

$$F^{t_1}_{1,Cox} = -\frac{\pi}{4}\frac{\ln(\delta)}{\sqrt{\lambda_1\lambda_2}}\left[\frac{6}{R_1(3\lambda_1+2\lambda_2)}-\frac{6}{R_1^2\lambda_1(3\lambda_1+2\lambda_2)}-4\right], \tag{2.14a}$$

$$\left(T^{t_1}_{2,Cox}\right)_o = \frac{\pi}{4}\frac{\ln(\delta)}{\sqrt{\lambda_1\lambda_2}}\left[\frac{6}{R_1\lambda_1(3\lambda_1+\lambda_2)}\right]. \tag{2.14b}$$

Lateral translation along the x_2-axis:

$$F^{t_2}_{2,Cox} = -\frac{\pi}{4}\frac{\ln(\delta)}{\sqrt{\lambda_1\lambda_2}}\left[\frac{6}{R_2(2\lambda_1+3\lambda_2)}-\frac{6}{R_2^2\lambda_2(2\lambda_1+3\lambda_2)}-4\right], \tag{2.15a}$$

$$F^{t_2}_{3,CB} = -\frac{3}{2}\frac{\pi\ln(\delta)}{\sqrt{\lambda_1\lambda_2}(\lambda_1+\lambda_2)}\left[2\sqrt{\lambda_2}\left(\frac{\kappa_1\lambda_1+3\kappa_3\lambda_2}{2\lambda_1+3\lambda_2}\right)\right.$$
$$\left.-\frac{3}{2}\frac{1}{R_2\sqrt{\lambda_2}}\left(\frac{\kappa_1(2\lambda_1+\lambda_2)+\kappa_3(2\lambda_1+7\lambda_2)}{2\lambda_1+3\lambda_2}\right)+\frac{\Gamma_1}{\lambda_1}+\frac{3\Gamma_3}{\lambda_2}\right], \tag{2.15b}$$

$$\left(T^{t_2}_{1,Cox}\right)_o = -\frac{\pi}{4}\frac{\ln(\delta)}{\sqrt{\lambda_1\lambda_2}}\left[\frac{6}{R_2\lambda_2(2\lambda_1+3\lambda_2)}\right]. \tag{2.15c}$$

Direct approach along the x_3-axis without rotation:

$$\left(T^{t_3}_{1,CB}\right)_o = -\frac{9}{4}\frac{\pi\ln(\delta)}{\sqrt{\lambda_1\lambda_2}(\lambda_1+\lambda_2)}\left[\frac{\kappa_1(2\lambda_1+\lambda_2)+\kappa_3(2\lambda_1+7\lambda_2)}{\sqrt{\lambda_2}(2\lambda_1+3\lambda_2)}\right], \tag{2.16a}$$

$$F^{t_3}_{2,CB} = -\frac{3}{2}\,\frac{\pi\ln(\delta)}{\sqrt{\lambda_1\lambda_2}(\lambda_1+\lambda_2)}\,\left[2\sqrt{\lambda_2}\,\left(\frac{\kappa_1\lambda_1+3\kappa_3\lambda_2}{2\lambda_1+3\lambda_2}\right)\right.$$
$$\left.-\frac{3}{2}\,\frac{1}{R_2\sqrt{\lambda_2}}\,\left(\frac{\kappa_1(2\lambda_1+\lambda_2)+\kappa_3(2\lambda_1+7\lambda_2)}{2\lambda_1+3\lambda_2}\right)+\frac{\Gamma_1}{\lambda_1}+\frac{3\Gamma_3}{\lambda_2}\right], \qquad (2.16b)$$

$$F^{t_3}_{3,Cox} = -\frac{3\pi}{\delta}\,\left[\frac{1}{\sqrt{\lambda_1\lambda_2}(\lambda_1+\lambda_2)}\right]. \qquad (2.16c)$$

In (2.12)–(2.16), $\lambda_1=(2R_1)^{-1}$ and $\lambda_2=(2R_2)^{-1}$, where R_1 and R_2 are the principle radii of curvature of the particle's surface at its closest approach to a wall; δ is the gap between the particle and the lower or upper wall at the point of closest approach. The variables κ_1, κ_3, Γ_1, Γ_3 are as defined in Cox (1974) and Claeys & Brady (1989), which, for our problem of an ellipsoid and a plane wall, yields

$$R_1 = -a^2 f^*, \qquad (2.17a)$$

$$R_2 = -\left(\frac{\cos^2\beta}{b^2}+\frac{\sin^2\beta}{c^2}\right)^{-1} f^*, \qquad (2.17b)$$

$$\kappa_1 = -\frac{\cos\beta\sin\beta}{2f^{*2}}\,\frac{1}{\lambda_1(\lambda_2)^{1/2}}\,\left(\frac{1}{c^2}-\frac{1}{b^2}\right)\,\frac{1}{a^2}, \qquad (2.17c)$$

$$\kappa_3 = -\frac{\cos\beta\sin\beta}{2f^{*2}}\,\frac{1}{(\lambda_2)^{3/2}}\,\left(\frac{1}{c^2}-\frac{1}{b^2}\right)\,\left(\frac{\cos^2\beta}{b^2}+\frac{\sin^2\beta}{c^2}\right), \qquad (2.17d)$$

$$\Gamma_1 = \kappa_1\lambda_1\,(\lambda_2)^{1/2}, \qquad (2.17e)$$

$$\Gamma_3 = \kappa_3\,(\lambda_2)^{3/2}, \qquad (2.17f)$$

where

$$f^* = \frac{y^*\cos\beta\sin\beta+(z^*-z^c)\sin^2\beta}{b^2}+\frac{-y^*\sin\beta\cos\beta+(z^*-z^c)\cos^2\beta}{c^2}, \qquad (2.17g)$$

$$y^* = y'\cos\beta - z'\sin\beta, \qquad (2.17h)$$

$$\left(z^*-z^c\right) = y'\sin\beta + z'\cos\beta, \qquad (2.17i)$$

$$y' = -\frac{b\sin\beta}{\sqrt{\sin^2\beta+\cos^2\beta(c^2/b^2)}}, \qquad (2.17j)$$

$$z' = y'\,\frac{c^2}{b^2}\,\frac{\cos\beta}{\sin\beta}, \qquad (2.17k)$$

with the prime notation referring to figure 2 and the * notation indicating the point of closest approach to a wall.

Analytical calculation of the $O(\ln\delta)$-correction to $F^{t_3}_3$, however, has met with formidable difficulties. Instead, we wrote a special one-wall boundary-integral code in the resistance formulation using the representation of Hebeker (1986), capable of accurately calculating $F^{t_3}_3$ for very small separations and avoiding inversion of ill-conditioned matrices. The one-wall near-contact results for this term can be represented as $F^{t_3}_3=(F^{t_3}_3)_{Cox}+bm\ln(\delta)+O(1)$, where the numerical coefficient m is a function only of the particle type (prolate spheroid or oblate spheroid), aspect ratio, and inclination angle. The values of m can be found by fitting

$F_3^{t_3} - F_{3,Cox}^{t_3} = bm\ln(\delta) + O(1)$ to boundary-integral results. The methodology of obtaining m, as well as the values for m for the range of β needed in dynamic simulations, are shown in figure 4(a–d) for prolate spheroids with $b/a = 2.5$ and oblate spheroids with $b/a = 0.4$. In addition, we confirmed the correctness of all the newly derived formulae (2.12b), (2.15b), (2.16a) and (2.16b) by comparison with boundary-integral calculations. As an example, figure 4(e) shows the comparison of $F_3^{t_2}$ and $\Delta F_{3,OW}^{t_2}$ for one-wall boundary-integral calculations for a prolate spheroid in the range $0.01 \leqslant \delta/b \leqslant 0.025$. While $F_3^{t_2}$ grows logarithmically, $\Delta F_{3,OW}^{t_2}$ remains $O(1)$ as $\delta/b \to 0$.

In order to be used in dynamic simulation of a spheroid between two walls, the analytical formulae (2.12)–(2.16), which describe motion in terms of the point of closest approach to the wall, must be transformed to describe motion of the particle centre (Appendix B). Five of the non-zero resistance coefficients ($T_3^{t_1}$, $T_3^{r_2}$, $T_2^{r_3}$, $T_3^{r_3}$, and $F_1^{r_3}$) and the six non-zero Poiseuille flow coefficients shown in (2.11) do not contain singularities and are tabulated as calculated by the boundary-integral simulation. Certain pairs of resistance coefficients can be related by the Lorentz reciprocal theorem, which alleviates some numerical errors associated with direct-approach motion (i.e. motion directly towards a wall). For example, calculation of the resistance coefficient $F_2^{t_3}$ (the force along x_2 due to translation along x_3) suffers from ill-conditioning when the mobility matrix $\boldsymbol{M}$ is numerically inverted to the resistance matrix $\boldsymbol{R}$. Errors associated with this ill-conditioning can be alleviated by using $F_3^{t_2}$ instead of $F_2^{t_3}$, and, hence, $\Delta F_3^{t_2}$, instead of $\Delta F_2^{t_3}$, in the tabulation. Similarly, ill-conditioned resistance coefficients $\Delta F_2^{r_1}$, $\Delta F_3^{r_1}$, $\Delta F_1^{r_2}$, $T_3^{r_2}$, and $F_1^{r_3}$, are replaced by $\Delta T_1^{t_2}$, $\Delta T_1^{t_3}$, $\Delta T_2^{t_1}$, $T_2^{r_3}$, and $T_3^{t_1}$, respectively.

To tabulate resistance coefficients for use in dynamic simulations, the boundary-integral results are obtained for a range of d/H and β that covers the applicable parameter space, with $d_{\max}/H = 0.5$, since cases with $d/H > 0.5$ are mirror images of those with $d/H < 0.5$. For spheroids with a dimensionless major axis length less than unity, tabulation for the prolate spheroid is in the range $0 \leqslant \beta \leqslant \pi/2$, with the range $\pi/2 \leqslant \beta \leqslant \pi$ for an oblate spheroid. For larger particles, the tabulation range in β is limited by the physical constraints that the particle does not overlap the walls (for example, $0 \leqslant \beta \leqslant \beta_{\max}$ for a prolate spheroid, where $\beta_{\max} = \arcsin\sqrt{(1-4c^2)/4(b^2-c^2)}$). In addition, a reliable range of tabulating the smooth Δ-coefficients was limited by $\delta_{LW}/H \geqslant 0.02$ for particles with major axis length $\geqslant 0.8$, and by $\delta_{LW}/H \geqslant 0.01$ for smaller particles with $\max(2a/H,\ 2b/H) = 0.4$; for smaller separations, the Δ-coefficients remain essentially constant. The 13 Δ-coefficients are obtained and tabulated for each β_j and d_i/H, as are the six non-zero Poiseuille flow coefficients (2.11) and the five non-singular resistance coefficients. Tabulation for a single particle size and shape takes a few days for a 30×20 mesh (in β and d/H) and 8640 triangles on a PC, resulting in a total of 7200 boundary-integral solutions. Once tabulated, however, these data can be used for very efficient dynamic simulations with arbitrary initial conditions and are valid to arbitrarily small separations, as described in the next section. The tabulation stage could be made considerably faster by a new Taylor-expansion technique for the smooth part of the Green's function, $\hat{G}_i^k(\boldsymbol{x};\boldsymbol{y})$, about the particle centre (Griggs, Zinchenko & Davis 2006). This recent improvement, however, was not incorporated in the present work.

2.6. *Dynamic simulation methodology*

To run the dynamic simulation, the initial configuration for a given particle is chosen by setting d_0/H, β_0, and φ_0, where d_0/H, β_0, and φ_0 are the initial values for these parameters (figure 1). The resistance coefficients are interpolated from the table in

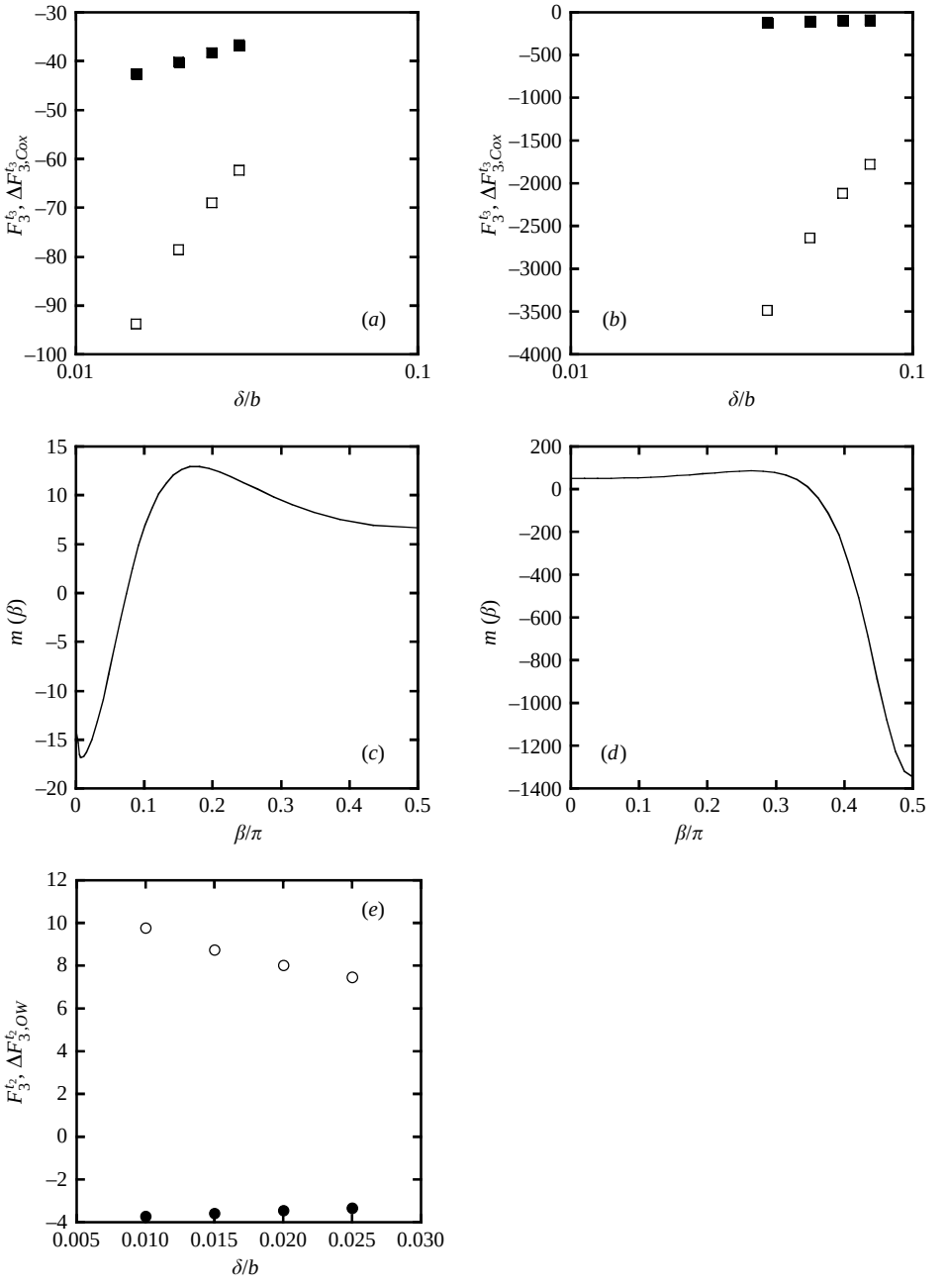

FIGURE 4. Boundary-integral results for resistance coefficients: (*a*) $F_3^{t_3}$ (□) and $F_3^{t_3} - F_{3,Cox}^{t_3} = mb\ln(\delta) + n$ (■) for $0.015 \leqslant \delta/b \leqslant 0.03$ for a prolate spheroid with $b/a = 2.5$ near a single wall, with $N_\triangle = 20480$; (*b*) $F_3^{t_3}$ (□) and $F_3^{t_3} - F_{3,Cox}^{t_3} = mb\ln(\delta) + n$ (■) for $0.0375 \leqslant \delta/b \leqslant 0.075$ for an oblate spheroid with $b/a = 0.4$ near a single wall, with $N_\triangle = 20480$; (*c*) $m(\beta)$ for a prolate spheroid near a single wall with $b/a = 2.5$; (*d*) $m(\beta)$ for an oblate spheroid near a single wall with $b/a = 0.4$; (*e*) $F_3^{t_2}$ (○) and $\Delta F_{3,OW}^{t_2}$ (●) for a prolate spheroid near a single wall with $b/a = 2.5$ for $0.01 \leqslant \delta/b \leqslant 0.25$.

β and d/H for the initial and subsequent configurations. For each Δ-coefficient, the corresponding lubrication formula is added for both the lower-wall and upper-wall contributions. These Δ-coefficients, along with the non-singular resistance coefficients, are inserted into the resistance matrix of (2.11), which is numerically inverted (2.10) at each timestep to obtain the mobility formulation. The translational and rotational velocities (U_i'', Ω_i'') are obtained through $\mathscr{U} = -\boldsymbol{M}\mathscr{F}^p$, and the differential equations of particle motion take the form

$$\frac{\mathrm{d}\beta}{\mathrm{d}t} = \Omega_1'', \tag{2.18a}$$

$$\frac{\mathrm{d}\varphi}{\mathrm{d}t} = \Omega_3'' - \Omega_2'' \tan\beta, \tag{2.18b}$$

$$\frac{\mathrm{d}x_1^c}{\mathrm{d}t} = U_1'' \sin\varphi + U_2'' \cos\varphi, \tag{2.18c}$$

$$\frac{\mathrm{d}x_2^c}{\mathrm{d}t} = -U_1'' \cos\varphi + U_2'' \sin\varphi, \tag{2.18d}$$

$$\frac{dx_3^c}{dt} = U_3''. \tag{2.18e}$$

The location and orientation of the particle is then updated using a first-order Euler scheme with a sufficiently small timestep proportional to the square root of the smallest gap from the walls, $\sqrt{\delta_{\min}}$. A first-order scheme and timestep scaling $\Delta t \sim \sqrt{\delta_{\min}}$ are used to ensure that the particle does not physically overlap the wall, which can occur with higher-order schemes, even with lubrication contributions included. Timesteps become very small when the particle is in close proximity to the walls, but our dynamic simulation is still very fast. This process can be repeated for hundreds of thousands of dimensionless timesteps in seconds of CPU time to obtain the particle trajectory and instantaneous particle velocities at any subsequent time for a given initial configuration. In the dynamic simulation code, it is assumed that the particle position, d/H, and inclination angle, β, may be outside the tabulation range (§ 2.5). In such cases, the necessary particle velocities are simply related to those in the tabulation range by symmetry properties.

3. Results and discussion

Three prolate (rod-like) spheroids and one oblate (disk-like) spheroid were chosen for study in this work. Spheroids, in which two of the principal axes have equal lengths, were chosen rather than ellipsoids, to limit the number of parameters. For most results, a minimum gap of $\delta_{LW,0}/H$, $\delta_{UW,0}/H = 1 \times 10^{-4}$ was chosen based on obtaining a physically relevant minimum gap of 0.01 μm for an application in which the channel height is 100 μm (a typical order of magnitude for the channel height for many microfluidics applications). Due to inclusion of the asymptotic lubrication formulae, the simulation data are accurate to smaller gaps (e.g. as shown in selected results in § 3.2.1), but extremely small gaps would not have physical significance, since a model with surface roughness and contact forces would then be needed to describe the particle motion (Smart, Beimfohr & Leighton 1993; Zhao, Galvin & Davis 2002). Dynamic simulations can yield β and φ outside the range $|\Delta\beta_0|, |\Delta\varphi_0| \leqslant 2\pi$, but since the motion is periodic, these results are simply multiples of results in the given range. Results are presented using the original coordinate system of figure 1.

3.1. *Spheroids with major axis length less than channel height*

The two prolate spheroids studied with major axes less than the channel height have $b/a = 2.5$ and $2b/H = 0.4$ or 0.8, respectively. The oblate spheroid studied has

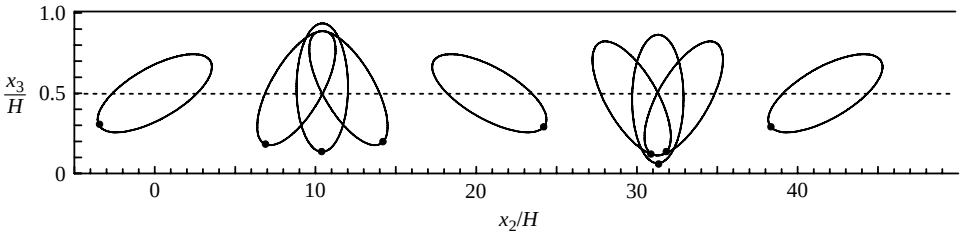

FIGURE 5. Two-dimensional projections in the $x_1 = 0$ plane for oscillating motion of a prolate spheroid with $b/a = 2.5$ and $2b/H = 0.8$ for $\varphi = \pi/2$, $d_0/H = 0.5$ and $\beta_0 = \pi/6$. The centre location is scaled as $(x_1^c, 0.1x_2^c, x_3^c)$ to allow the motion of the particle to be easily observed while maintaining the proper particle shape. Projections are shown at $\hat{t} = tU_c/H = 0$, 9.85, 11.90, 13.97, 23.78, 33.68, 35.75, 37.80, and 47.65 (left to right). The dot was added to indicate particle orientation.

$2a/H = 2c/H = 0.8$ and $b/a = 0.4$. A particle with a major axis length that is less than the channel height can fully rotate in the channel even when it is aligned with its major axis confined to the $x_1 = 0$ plane ($\varphi = \pi/2$). The motions observed for spheroids with dimensionless major axes less than unity are (i) steady translation in the x_2-direction without rotation, with the particle centre on the midplane of the channel; (ii) steady translation along x_2 with rotation when $\varphi_0 = 0$; (iii) oscillating motion (*a*) in two dimensions, in which β ranges from β_0 to $\pi - \beta_0$ or (*b*) in three dimensions, in which the particle centre location, d/H, and the angles β and/or φ oscillate about their starting values; and (iv) tumbling motion (*a*) in two dimensions, in which β progresses clockwise (as viewed from the positive x_1-axis) for initial centre locations below the midplane of the channel, or (*b*) in three dimensions, in which both β and φ take on both positive and negative values during a period of motion. The uniformity of the flow field along the x_1-axis means that $U_1 = 0$ for all cases. The prolate spheroid for which detailed results are presented is the larger of the two, with its major axis equal to 80% of the channel depth.

3.1.1. *Prolate spheroid with $2b/H = 0.8$ and its axis of symmetry in the $x_1 = 0$ plane*

Setting $\varphi_0 = \pi/2$ allows motion of type (i), (iii) (a) and (iv) (a) mentioned above to occur, but the combination of $H\Omega_2'/U_c = H\Omega_3'/U_c = 0$ (preventing changes in φ) and $U_1/U_c = 0$ (preventing translation along x_1) restricts the prolate spheroid's major axis to the $x_1 = 0$ plane, where $\varphi = \pi/2$. A steady-state motion of type (i) is observed for $d_0/H = 0.5$ and $\beta_0 = 0$ or $\beta = \pi/2$, with the only non-zero velocity being U_2/U_c. For $d_0/H = 0.5$ and $\beta_0 \neq 0$ or $\pi/2$, an oscillatory motion of type (iii) (a) occurs, in which β and d/H oscillate about their starting values, in part due to a non-zero lift velocity ($U_3/U_c \neq 0$) that occurs for the initial configuration. Two-dimensional oscillatory motions also occur for certain combinations of $d_0/H \neq 0.5$ and $\beta_0 \neq 0$ near the midplane of the channel. However, since all oscillatory trajectories for $\varphi = \pi/2$ are periodic and the amplitude of the oscillations is symmetric about the midplane of the channel, oscillating trajectories that begin off the midplane are identical to other trajectories that begin in the midplane. For example, the oscillating trajectory for $\beta_0 = \pi/6$ and $d_0/H = 0.5$ is the same as that for $\beta_0 = 0.695$ and $d_0/H = 0.48$, but it begins at a different point along the periodic trajectory. Particle projections in the $x_1 = 0$ plane as a function of the particle's centre location along the channel length scaled by the channel height, x_2^c/H, are shown in figure 5 for a prolate spheroid with $b/a = 2.5$ and $2b/H = 0.8$ oscillating about $d/H = 0.5$ for $d_0/H = 0.5$ and $\beta_0 = \pi/6$. For this oscillatory motion, the spheroid first rotates in the counter-clockwise direction

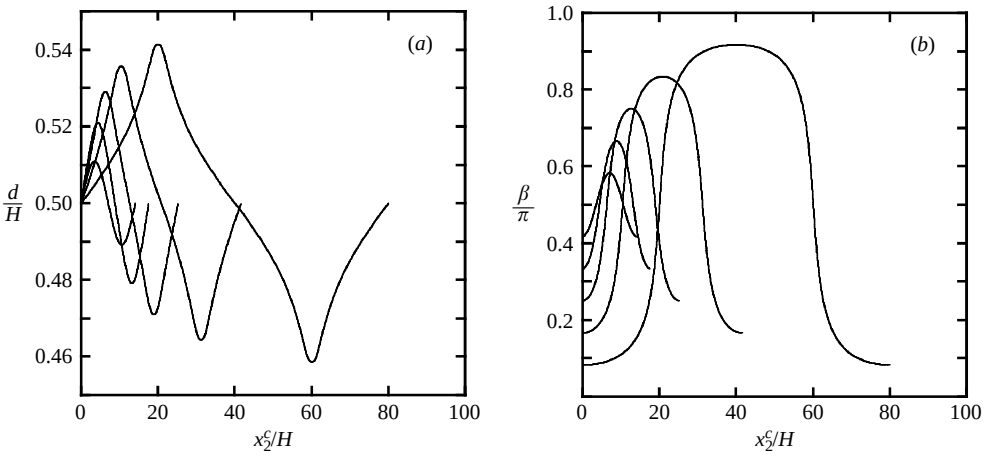

FIGURE 6. Prolate spheroid with $b/a = 2.5$ and $2b/H = 0.8$ for two-dimensional oscillating motion with $\varphi = \pi/2$, $d_0/H = 0.5$ and $\beta_0 = \pi/12$, $\pi/6$, $\pi/4$, $\pi/3$, and $5\pi/12$: (*a*) d/H vs. x_2^c/H (right to left at minimum d/H for each curve), and (*b*) β/π vs. x_2^c/H (bottom to top at $\beta_0 = 0$).

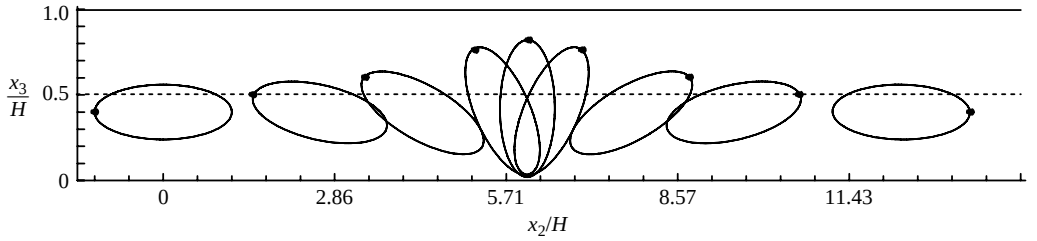

FIGURE 7. Two-dimensional projections in the $x_1 = 0$ plane for tumbling motion of a prolate spheroid with $b/a = 2.5$ and $2b/H = 0.8$ for $\varphi = \pi/2$, $d_0/H = 0.4$ and $\beta = 0$ for the range $0 \leqslant \beta/\pi \leqslant 1$ (half-period length). The centre location is scaled as $(x_1^c, 0.35x_2^c, x_3^c)$ to allow the motion of the particle to be easily observed while maintaining the proper particle shape. Projections are shown along x_2^c/H at $\hat{t} = tU_c/H = 0$, 2.85, 4.77, 6.40, 6.96, 7.51, 9.14, 11.05, and 14.10 (left to right). The dot was added to indicate particle orientation.

(as viewed along the positive x_1-axis) until it reaches $5\pi/6$, at which point the rotation becomes clockwise to return the spheroid to its initial orientation. The changes in various parameters for a range of cases with $d_0/H = 0.5$ and $\beta_0 \neq 0$ are shown in figure 6. The period length (defined as the time it takes for the spheroid to return to β_0, d_0/H and φ_0) decreases with increasing β_0 for $\varphi = \pi/2$, due to increased interactions of the prolate spheroid with the walls for larger β_0. For these oscillating cases, $\beta_0 \leqslant \beta \leqslant (\pi - \beta_0)$ is experienced as the dynamic simulation progresses.

For $\varphi = \pi/2$, $\beta_0 = 0$ and $d_0/H \neq 0.5$, a two-dimensional tumbling motion of type (iv) (a) occurs, in which β progresses in a clockwise direction (decreases) for $d_0/H < 0.5$ and d/H changes in a periodic fashion, with the length of one period defined as $|\Delta\beta| = 2\pi$. Certain other starting values of β_0 can also result in tumbling trajectories, but these trajectories contain $\beta = 0$, meaning they are duplicates of trajectories with different d_0/H, β_0. Figure 7 shows the particle projections in the $x_1 = 0$ plane as a function of x_2^c/H for a case with $\beta_0 = 0$ and $d_0/H = 0.4$, in which it can be seen that the rate of change in β is greater for smaller δ_{LW}/H, due to an increased interaction with the wall for these smaller spheroid–wall gaps. In this two-dimensional tumbling

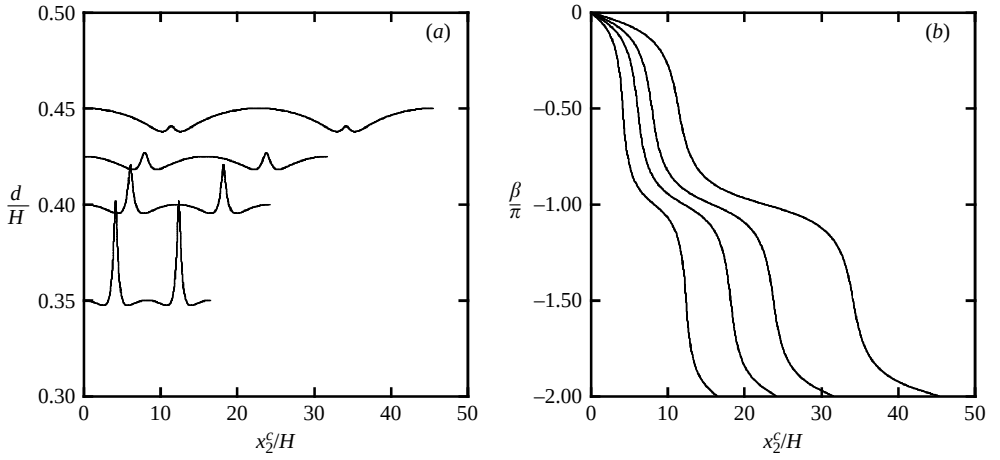

FIGURE 8. Prolate spheroid with $b/a = 2.5$ and $2b/H = 0.8$ for two-dimensional tumbling motion with $\varphi = \pi/2$, $\beta_0 = 0$, $d_0/H = 0.35$, 0.40, 0.425, and 0.45: (*a*) d/H vs. x_2^c/H (bottom to top), and (*b*) β/π vs. x_2^c/H (left to right).

motion, the period length for tumbling motion increases for larger d_0/H, as shown in figure 8 for $\beta_0 = 0$ and $0.35 \leqslant d_0/H \leqslant 0.45$.

3.1.2. *Prolate spheroid with* $2b/H = 0.8$ *and its axis of symmetry not confined to the* $x_1 = 0$ *plane*

For these cases, the particle rotates freely, such that the major axis does not remain confined to the $x_1 = 0$ plane. For $d_0/H = 0.5$, $\beta_0 = 0$ or $\pi/2$, and any value of φ_0, a steady motion of type (i) with $U_2/U_c > 0$ occurs, as expected from the symmetry of the parallel-plate Poiseuille flow about these midplane locations. This type (i) steady motion also occurs for $d_0/H = 0.5$, $\varphi_0 = 0$, and any value of $\beta_0 \neq \pi/2$. For $\beta_0 = \varphi_0 = 0$ and $d_0/H < 0.5$, a steady motion of type (ii) with $U_2/U_c > 0$ and $H\Omega_2'/U_c < 0$ yields a clockwise rotation of the spheroid about its major axis, which is parallel to the $x_3 = 0$ plane. For cases with $\beta_0 = \pi/2$ and $d_0/H \neq 0.5$, the initial condition is an unstable position in which a small disturbance causes the major axis of the prolate spheroid to rotate away from its alignment along the x_3-axis. This rotation results in a rapid change in φ based on the direction in which the spheroid rotates off the x_3-axis, since φ is defined as the angle between the projection of the particle's axis of symmetry in the $x_3 = 0$ plane and the x_1-axis and has no meaning when $\beta = \pi/2$. The prolate spheroid quickly reaches a stable motion in which $\varphi = j\pi/2$, where j is an integer such that the type (iv) (a) tumbling motion observed is the same as observed for a prolate spheroid with $\varphi_0 = \pi/2$ (which has $j = 1$). Small numerical instabilities during the course of the dynamic simulation (which arise from table interpolation) allow j to change due to rapid changes in φ, but the particle quickly realigns with its major axis in the $x_1 = 0$ plane, yielding a stable trajectory of type (iv) (a) motion observed for cases with $\varphi = \pi/2$ described previously (see figures 7 and 8).

A three-dimensional oscillating motion of type (iii) (b) is observed for $\varphi_0 \neq \pi/2$ and d_0/H in or near the midplane of the channel (similar to § 3.1.1), with these oscillating trajectories all passing through $\varphi = 0$. In these situations, the parameters d/H, β, and φ all oscillate, even for midplane cases with $\beta_0 \neq 0$, $\pi/2$ and $\varphi_0 \neq 0$. All three dimensionless rotational components of the velocity are on the order of 0.1, causing changes in both β and φ as the simulation progresses, as shown by the

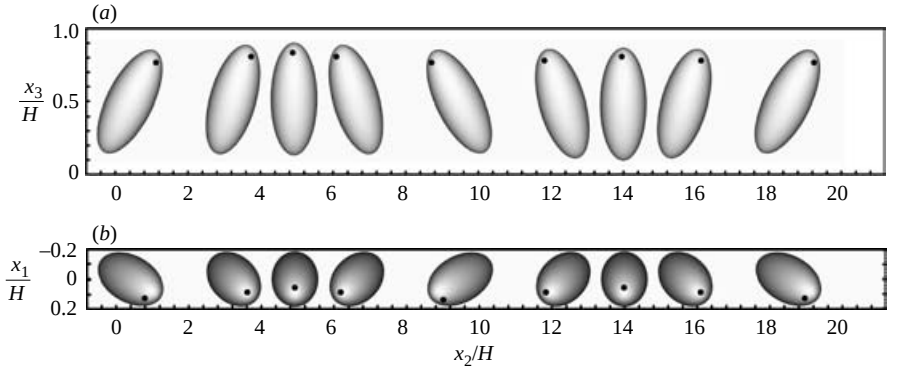

FIGURE 9. Three-dimensional images for oscillating motion of a prolate spheroid with $b/a = 2.5$ and $2b/H = 0.8$ for $\beta_0 = \varphi_0 = \pi/3$, $d_0/H = 0.5$, and scaling of the centre location as $(x_1^c, 0.25x_2^c, x_3^c)$, with images at $\hat{t} = tU_c/H = 0$, 3.48, 5.61, 7.76, 11.24, 14.73, 16.85, 18.98, and 22.46 shown (*a*) from the side and (*b*) from the top. The dot (different dot in each part) was added to indicate particle orientation.

three-dimensional particle images for $\beta_0 = \varphi_0 = \pi/3$ and $d_0/H = 0.5$ in figure 9. As with the two-dimensional oscillating cases in § 3.1.1, the period length increases with decreasing β_0 for the same d_0/H and φ_0. Figure 10 shows the results for $d_0/H = 0.5$ and constant $\beta_0 = \pi/3$ with a range of φ_0. An increase in φ_0 yields a shorter period length and a larger range of oscillations in d/H, β, φ and U_2/U_c. The period length is defined as the time it takes for the particle to complete one full oscillation and return to its starting condition, which is dependent on φ, rather than β, for these oscillating cases with $\varphi_0 \neq \pi/2$. The translational velocity in the primary flow direction, U_2/U_c, decreases only slightly for an increase in β, since the particle does not oscillate very far away from the midplane, and, hence, does not have a significantly increased interaction with the walls. Even for $\varphi_0 = \pi/3$, the variation in U_2/U_c is only about $\pm 2\%$ from the average. For these oscillating cases with d_0/H in or near the midplane, $\beta > 0$ for the entire simulation. This result can be more easily observed by noting that the end of the spheroid that is projected out of the page in figure 9 remains above d/H for the entire sequence of images.

A three-dimensional tumbling motion of type (iv) (b) is observed for $\varphi_0 \neq \pi/2$ and d_0/H farther from the midplane. Figure 11 shows three-dimensional particle images for $\beta_0 = \varphi_0 = \pi/3$ and $d_0/H = 0.45$. As can be seen from the projections, the tip of the particle projected out of the page begins above the centre of the particle but passes below the centre as time progresses, which is indicative of type (iv) (b) motion. Figure 12 shows results for $d_0/H = 0.45$, constant $\varphi_0 = \pi/3$ and variations in β_0. Unlike the oscillating cases discussed previously in §§ 3.1.1–3.1.2, keeping d_0/H and φ_0 constant while changing β_0 yields a period length that decreases with decreasing β_0. For constant d_0/H and β_0 (not shown for space considerations), an increase in φ_0 gives a shorter period length and larger oscillations in β, φ, and d/H. The period length decreases with a decrease in β_0 or an increase in φ_0, with a change in β_0 having a more pronounced effect upon the period length (figure 12). For both angular parameters β and φ in these three-dimensional tumbling cases, the maximum values of β and φ tends to be slightly larger than the initial value, such that the maximum value of β or φ increases with an increase in β_0 or φ_0. As β_0 increases and/or φ_0 decreases, the deviation of d/H from d_0/H also increases. The value of β_0 has a greater effect upon this variance than does φ_0, since the increase in β_0 causes the edge

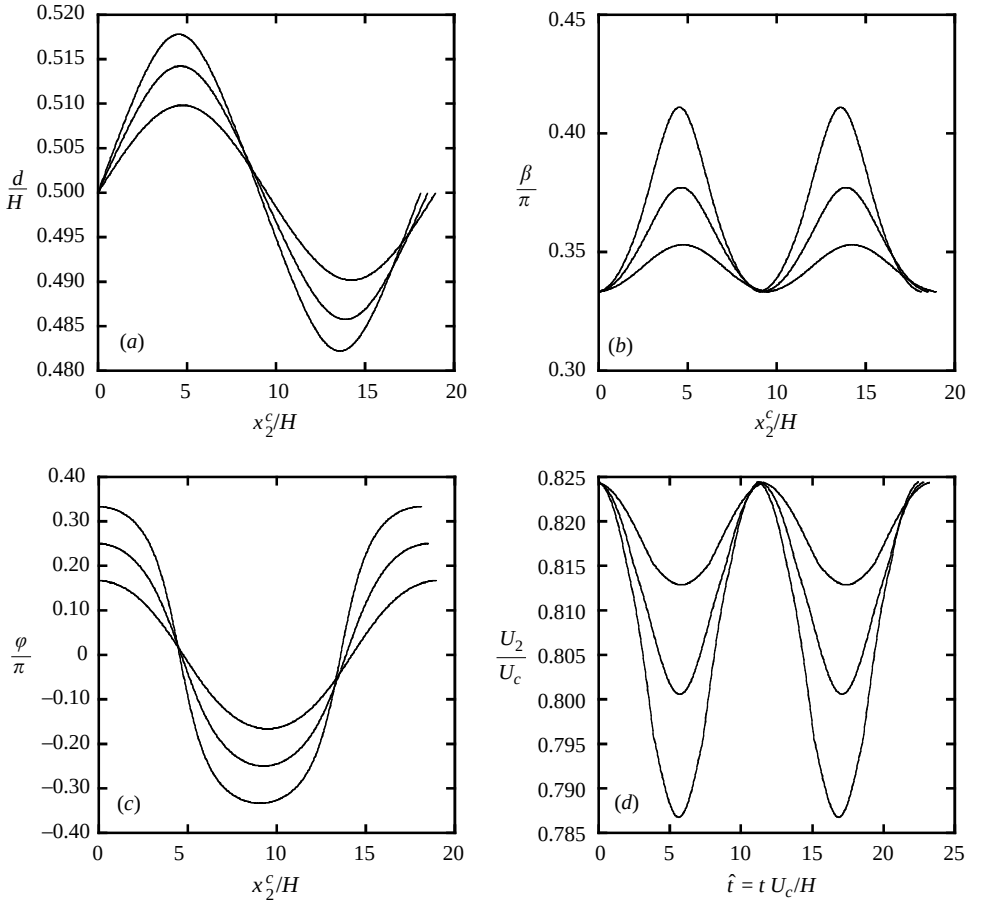

FIGURE 10. Prolate spheroid with $b/a = 2.5$ and $2b/H = 0.8$ for three-dimensional oscillating motion with $d_0/H = 0.5$, $\beta_0 = \pi/3$, $\varphi_0 = \pi/6$, $\pi/4$, and $\pi/3$: (*a*) d/H vs. x_2^c/H (bottom to top at $x_2^c/H = 5$), (*b*) β/π vs. x_2^c/H (bottom to top at $x_2^c/H = 5$), (*c*) φ/π vs. x_2^c/H (bottom to top at $x_2^c/H = 0$), (*d*) U_2/U_c vs. $\hat{t} = tU_c/H$ (top to bottom at $x_2^c/H = 5$).

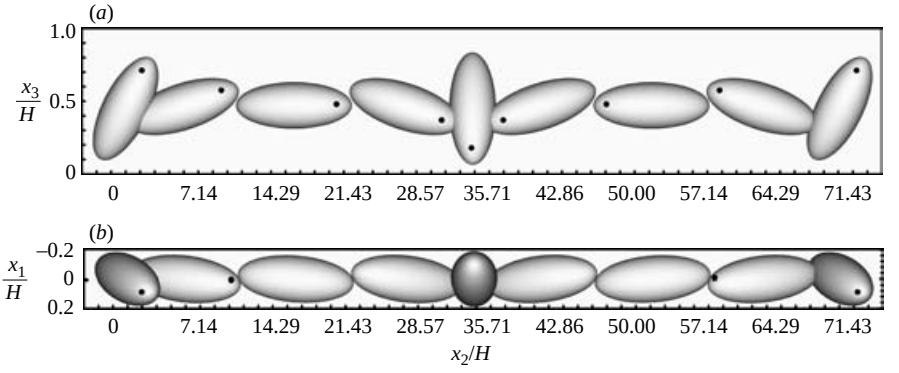

FIGURE 11. Three-dimensional images for tumbling motion of a prolate spheroid with $b/a = 2.5$ and $2b/H = 0.8$ for $\beta_0 = \varphi_0 = \pi/3$, $d_0/H = 0.45$, and scaling of the centre location as $(x_1^c, 0.07x_2^c, x_3^c)$, with images at $\hat{t} = tU_c/H = 0$, 6.32, 17.68, 29.10, 36.64, 44.21, 55.62, 66.98, and 75.77 shown (*a*) from the side and (*b*) from the top. The dot was added to indicate particle orientation.

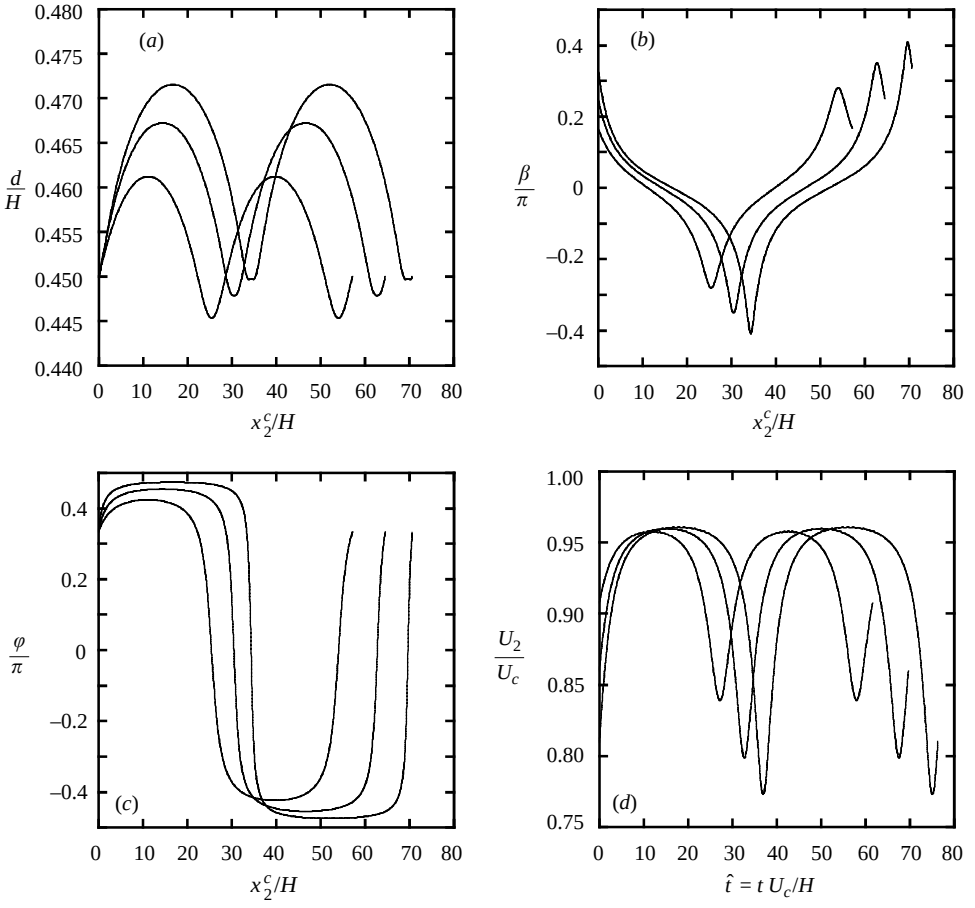

FIGURE 12. Prolate spheroid with $b/a = 2.5$ and $2b/H = 0.8$ for three-dimensional tumbling motion with $d_0/H = 0.45$, $\varphi_0 = \pi/3$ and $\beta_0 = \pi/6$, $\pi/4$, and $\pi/3$: (*a*) d/H vs. x_2^c/H (bottom to top at $x_2^c/H = 10$), (*b*) β/π vs. x_2^c/H (bottom to top at $x_2^c/H = 0$), (*c*) φ/π vs. x_2^c/H (bottom to top at $x_2^c/H = 10$), (*d*) U_2/U_c vs. $\hat{t} = tU_c/H$ (top to bottom at $x_2^c/H = 0$).

of the particle to be located closer to the walls of the channel whereas a change in φ_0 does not have a direct effect upon the particle spacing from the walls. Unlike the type (iii) (b) three-dimensional oscillating motion, in this type (iv) (b) three-dimensional tumbling motion, both β and φ oscillate about zero (figure 12), as evidenced by noting that the tip of the spheroid projected out of the page in figure 11 passes below the particle centre during the sequence of images. For this type (iv) (b) tumbling motion (figure 12), the variation in U_2/U_c is much larger than for the type (iii) (b) oscillating motions (figure 10), due to the increased interactions with the walls that arise from the larger changes in both β and d_0/H during a period of motion. The values for U_2/U_c also change more for a change in β_0 than a change in φ_0, since a change in β_0 yields larger changes in β than does a change in φ_0, subsequently causing more interactions of the particle with the channel walls.

3.1.3. *Comparison with Jeffery's solution*

An orbiting motion of a spheroid freely suspended in an unbounded shear flow is described by the classical solution of Jeffery (1922). According to this solution, all

d_0/H	β_0 (deg.)	φ_0 (deg.)	T_{ex}	T_∞
0.35	0	90	20.13	15.18
0.375	0	90	23.17	18.22
0.4	0	90	27.96	22.78
0.425	0	90	35.66	30.37
0.45	0	90	49.93	45.55
0.475	0	90	83.44	91.11
0.45	0	30	54.32	45.55
0.45	0	45	52.97	45.55
0.45	30	30	62.94	45.55
0.45	30	60	61.62	45.55
0.45	30	45	62.31	45.55
0.45	45	45	70.12	45.55
0.45	45	60	69.70	45.55
0.45	60	30	76.67	45.55
0.45	60	45	76.50	45.55

TABLE 1. Comparison of the period of orbiting motion between the present and Jeffery's solutions for a prolate spheriod with $b/a = 2.5$ and $2b/H = 0.8$.

orbiting motions, irrespective of the initial conditions, have the period $T_\infty = (2\pi/k)(e + 1/e)$, where k is the shear rate and e is the spheroid aspect ratio. Although Jeffery's solution does not include possible wall effects, it was found to be a useful approximation in a recent boundary-integral study (Pozrikidis 2005) of a spheroid's orbiting motion in a shear flow near a plane wall. The calculations of Pozrikidis (2005), although they do not directly incorporate lubrication effects, were performed in the range of strong particle–wall interactions where deviations from Jeffery's (1922) solution are expected. Nevertheless, the maximum difference in the period of motion from Jeffery's formula is only 20%.

In the present case of a channel flow, comparison with Jeffery's solution is conceptually more difficult, because the shear rate of the unperturbed flow varies across the channel (and is zero on the plane of symmetry), and the particle undergoes lateral migration. One approach would be to use the shear rate of the unperturbed flow at the average location of the particle centre along a trajectory in Jeffery's solution. Such a comparison, however, would make the analytical solution dependent on the results of our numerical simulations, Instead, we simply use the non-dimensional shear rate $k = 4(1 - 2d_0/H)$ of the Poiseuille flow at the *initial* position d_0 of the particle centre in Jeffery's solution. Table 1 presents comparisons of the period of orbiting motion between our exact numerical solution (T_{ex}) and Jeffery's solution (T_∞) for a prolate spheroid with an aspect ratio of $b/a = 2.5$ and $2b/H = 0.8$ (the geometry considered in the previous §§ 3.1.1 and 3.1.2) at different initial conditions d_0/H, β_0 and φ_0.

For trajectories starting from $\beta = 0$ and confined to the $x_1 = 0$ plane ($\varphi_0 = 90°$), Jeffery's formula underestimates the period of rotation most significantly when the particle is close to one wall (obviously because particle–wall interactions slow down rotation), but the error does not exceed 25%. As the initial particle–wall separation increases, Jeffery's solution becomes more accurate. However, for d_0/H very close to 0.5 (when both T_{ex} and T_∞ are large), the trend is reversed and Jeffery's formula

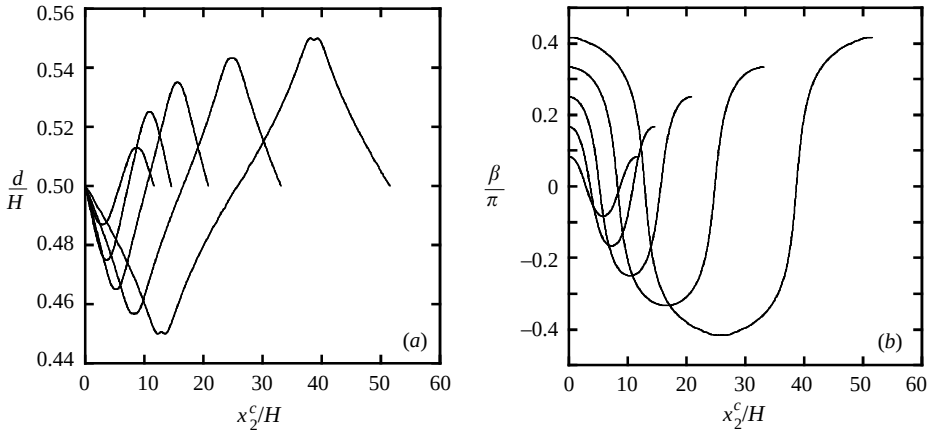

FIGURE 13. Oblate spheroid with $b/a = 0.4$ and $2b/H = 0.32$ for two-dimensional oscillating motion with $\varphi = \pi/2$, $d_0/H = 0.5$, and $\beta_0 = \pi/12$, $\pi/6$, $\pi/4$, $\pi/3$, and $5\pi/12$: (*a*) d/H vs. x_2^c/H (left to right at maximum d/H for each curve), (*b*) β/π vs. x_2^c/H (bottom to top at $x_2^c/H = 0$).

overestimates the period of rotation. The explanation is that, for d_0/H close to 0.5, the average value of d/H becomes smaller than the initial value d_0/H (see figure 8), so the particle centre tends to stay away from the range of nearly-zero shear rate, and the exact period of rotation T_{ex} is shorter than that from Jeffery's solution.

For general three-dimensional tumbling motions ($\varphi \neq 90°$), Jeffery's solution is a less successful approximation. The observed deviations from exact results for the period of rotation are as large as 41% (table 1) for $\varphi \neq 90°$.

3.1.4. *Oblate spheroid with* $2b/H = 0.32$ *and its axis of symmetry in the* $x_1 = 0$ *plane*

The oblate spheroid studied has its major axes less than the channel spacing, and $b/a = 0.4$. The projection of this spheroid in the $x_1 = 0$ plane is the same as that for the prolate spheroid with $2b/H = 0.8$, but since $2a/H = 2c/H = 0.8$ for this oblate spheroid, it has a larger volume than the prolate spheroid with equivalent major axis length (§§ 3.1.1–3.1.2). The inclination angle β is still defined as the angle of the particle's unique axis with respect to the $x_3 = 0$ plane, meaning that, for oblate spheroids, $\beta = \pi/2$ is the configuration with the particle's major axes parallel to the walls. When this spheroid has its unique axis confined to the $x_1 = 0$ plane, it experiences type (i), (iii) (a) and (iv) (a) motions. As with the small prolate spheroid of equivalent major axis length, steady-state motion of type (i) is encountered for $d_0/H = 0.5$, $\varphi = \pi/2$, and $\beta = 0$, $\pi/2$.

Oscillating motion of type (iii) (a) occurs for certain centre locations in/near the midplane of the channel with $\beta \neq 0$, $\pi/2$, while tumbling motion of type (iv) (a) occurs for centre locations further from the midplane. A set of two-dimensional oscillating trajectories with $d_0/H = 0.5$, $\varphi = \pi/2$, and various β_0 is shown in figure 13. (Two-dimensional particle projections are not shown for space considerations, since they are qualitatively the same as for the prolate spheroid in § 3.1.1.). The period length increases with increasing β, which is equivalent to the period length decreasing for increasing β for the corresponding prolate spheroid. The period length for the oscillating oblate spheroid is shorter than that of the oscillating prolate spheroid for the same d_0/H and equivalent β_0 (seen by comparing figure 13 and figure 6), since the larger surface area of the oblate spheroid causes it to oscillate faster than the prolate spheroid. As with the comparable prolate spheroid, oscillating trajectories that begin

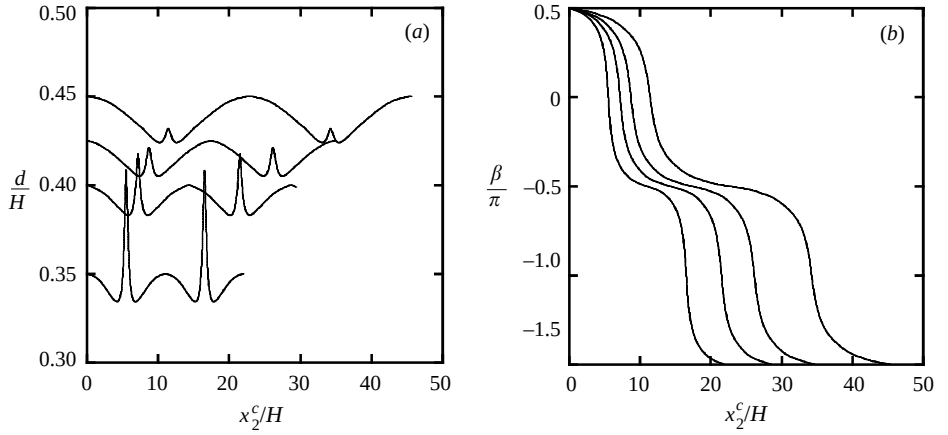

FIGURE 14. Oblate spheroid with $b/a = 0.4$ and $2b/H = 0.32$ for two-dimensional tumbling motion with $\varphi = \pi/2$, $\beta_0 = \pi/2$, $d_0/H = 0.35$, 0.40, 0.425, and 0.45: (*a*) d/H vs. x_2^c/H (bottom to top at $x_2^c/H = 0$), (*b*) β/π vs. x_2^c/H (left to right).

with the particle centre off the midplane coincide with trajectories that begin with the particle centre in the midplane.

Since tumbling motion for $\varphi = \pi/2$ occurs when a given trajectory includes the configuration with one of the spheroid's major axes (specifically, the major axis confined to the $x_1 = 0$ plane) parallel to the walls, type (iv) (a) tumbling motion occurs for oblate spheroid trajectories with $d_0/H \neq 0.5$ that include $\beta = \pi/2$. Figure 14 shows two-dimensional tumbling trajectories for $0.35 \leqslant d_0/H \leqslant 0.45$, demonstrating that (similar to § 3.1.1) the period length decreases with a decrease in d_0/H, due to the closer proximity of the particle to the lower wall. The period length of the prolate spheroid of § 3.1.1 is greater than that of this oblate spheroid for tumbling trajectories that begin near the midplane. In contrast, for smaller d_0/H, the oblate spheroid period length is greater than that of the prolate spheroid, with the difference in period length growing for smaller d_0/H. As the two spheroids are located closer to a wall, the larger volume of the oblate spheroid gives it an increased surface area in close proximity to the wall compared to the prolate spheroid, causing its period to be longer than that of the comparable prolate spheroid.

3.1.5. *Oblate spheroid with $2b/H = 0.32$ and its axis of symmetry not confined to the $x_1 = 0$ plane*

When the axis of rotation of this oblate spheroid is not confined to the $x_1 = 0$ plane, it experiences motions of type (i), (iii) (b), and (iv) (b). Steady-state motion of type (i) occurs for $d_0/H = 0.5$ and $\beta_0 = \pi/2$ (both major axes parallel to the $x_3 = 0$ plane), as well as for $d_0/H = 0.5$, $\varphi_0 = 0$, and $\beta_0 = 0$ (both major axes in the $x_1 = 0$ plane).

A three-dimensional oscillating motion of type (iii) (b) occurs for locations near the midplane. Figure 15 shows the three-dimensional particle images for $\beta_0 = \pi/6$, $\varphi_0 = \pi/3$, and $d_0/H = 0.5$. As with the prolate spheroid, three-dimensional oscillating motion of this oblate spheroid is demonstrated by noting that the oblate spheroid remains oriented such that the dot in figure 15 (added to indicate particle orientation) remains above the spheroid centre during the period of motion. Trajectories for $d_0/H = 0.5$ and a range of φ_0 are provided in figure 16, which shows that the period length decreases for an increase in φ_0. The period length also decreases for a decrease

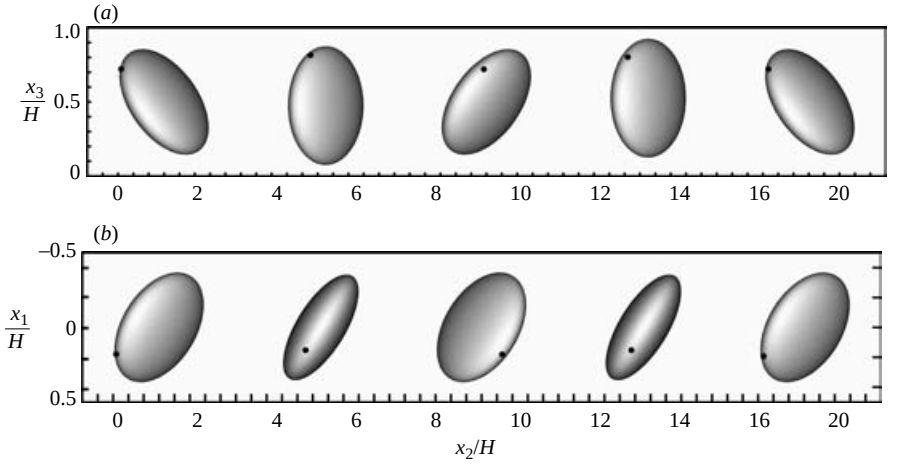

FIGURE 15. Three-dimensional images for oscillating motion of an oblate spheroid with $b/a = 0.4$ and $2b/H = 0.32$ for $\beta_0 = \pi/6$, $\varphi_0 = \pi/3$, $d_0/H = 0.5$, and scaling of the centre location as $(x_1^c, 0.25x_2^c, x_3^c)$, with images at $\hat{t} = tU_c/H = 0$, 5.31, 10.58, 15.90, and 21.21 shown (*a*) from the side and (*b*) from the top. The dot was added to indicate particle orientation.

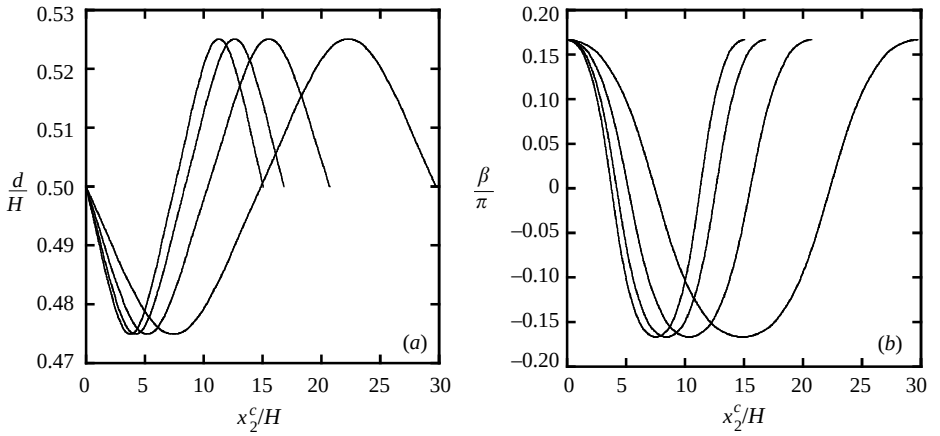

FIGURE 16. Oblate spheroid with $b/a = 0.4$ and $2b/H = 0.32$ for three-dimensional oscillating motion with $d_0/H = 0.5$, $\beta_0 = \pi/6$ and $\varphi_0 = \pi/6$, $\pi/4$, $\pi/3$, and $5\pi/12$: (*a*) d/H vs. x_2^c/H (right to left at maximum d/H for each curve), (*b*) β/π vs. x_2^c/H (right to left).

in β_0 (similar to the decrease in period length for an increase in β_0 observed in § 3.1.2, due to the definition of β as the inclination angle of the unique axis).

Three-dimensional tumbling motion of type (iv) (b) occurs for d_0/H further from the midplane of the channel, with a set of three-dimensional images shown in figure 17 for $\beta_0 = \pi/6$, $\varphi_0 = \pi/3$, and $d_0/H = 0.4$. As with the prolate spheroid, in three-dimensional tumbling, β and φ switch from positive to negative during a period, as evidenced by following the dot on the spheroid in figure 17. Figure 18 gives the changes in β and φ for a range of φ_0 with $d_0 = 0.4$ and $\beta_0 = \pi/6$. The shape of the centre location trajectory (not shown for brevity) is qualitatively similar for the cases presented in figure 18, being in the range $0.392 \leqslant d/H \leqslant 0.419$ for the four sets of initial conditions shown. The period length decreases for an increase in φ_0 or β_0. Similar to

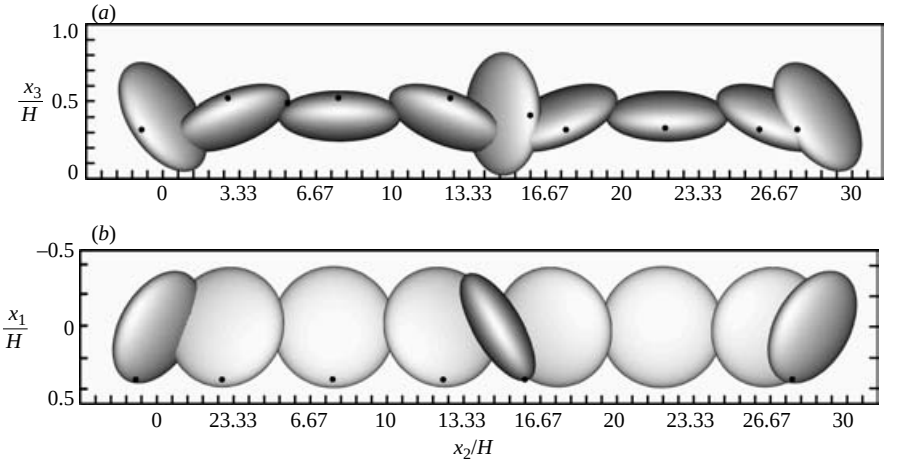

FIGURE 17. Three-dimensional images for tumbling motion of an oblate spheroid with $b/a = 0.4$ and $2b/H = 0.32$ for $\beta_0 = \pi/6$, $\varphi_0 = \pi/3$, $d_0/H = 0.4$, and scaling of the centre location as $(x_1^c, 0.15x_2^c, x_3^c)$, with images at $\hat{t} = tU_c/H = 0$, 3.88, 9.04, 14.19, 17.28, 20.38, 25.54, 30.69, and 32.97 shown (*a*) from the side and (*b*) from the top. The dot was added to indicate particle orientation.

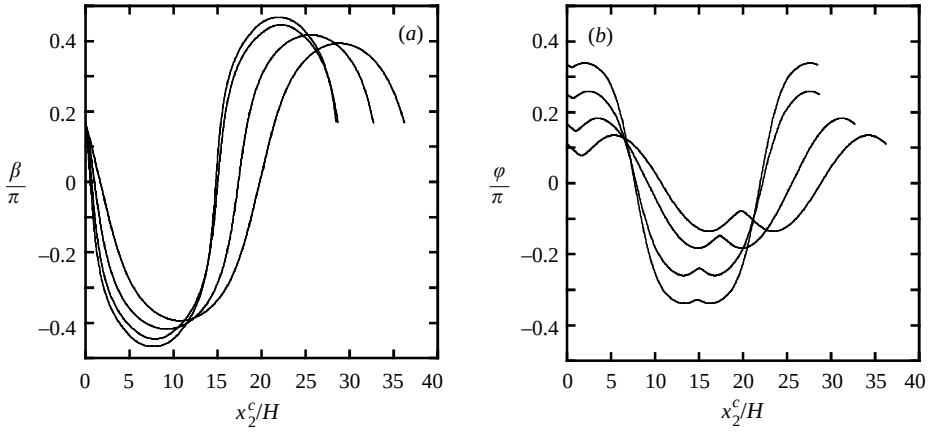

FIGURE 18. Oblate spheroid with $b/a = 0.4$ and $2b/H = 0.32$ for three-dimensional tumbling motion with $d_0/H = 0.4$, $\beta_0 = \pi/6$ and $\varphi_0 = \pi/9$, $\pi/6$, $\pi/4$, and $\pi/3$: (*a*) β/π vs. x_2^c/H (right to left at $\beta/\pi = 0.25$), (*b*) φ/π vs. x_2^c/H (bottom to top at $x_2^c/H = 0$).

the prolate spheroid in § 3.1.1, if a simulation is started with $\beta_0 = \pi/2$, φ will rapidly reach $\varphi = j\pi/2$, where j is an integer such that the type (iv) (a) motion observed is the same as observed for an oblate spheroid with $\varphi_0 = \pi/2$ (which has $j = 1$).

3.1.6. *Demarcation of tumbling and oscillating regions for axis of symmetry in the* $x_1 = 0$ *plane*

The type of two-dimensional motion experienced by a spheroid with its axis of rotation confined to the $x_1 = 0$ plane can be described by a phase-space diagram which indicates the combinations of d/H and β that yield tumbling or oscillating motions. Figure 19 shows the transition from oscillating motion of type (iii) (a) to

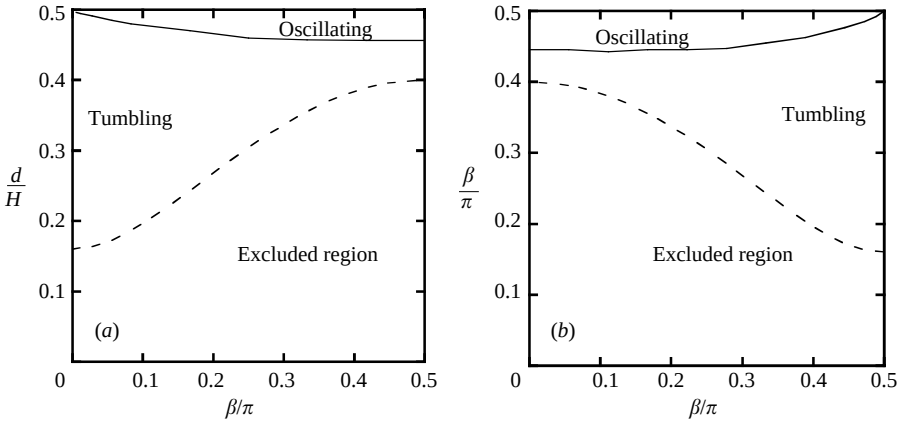

FIGURE 19. Phase-space diagrams for (*a*) a prolate spheroid with $b/a = 2.5$ and $2b/H = 0.8$ and (*b*) an oblate spheroid with $b/a = 0.4$ and $2b/H = 0.32$, for $\varphi = \pi/2$. The solid line demarcates the transition from oscillating to tumbling motion, while the dashed line indicates the centre location for the minimum δ_{LW}/H by physical constraints. Steady motion occurs for $d_0/H = 0.5$ and $\beta_0 = 0, \pi/2$.

tumbling motion of type (iv) (a) for combinations of β and d/H with $\varphi = \pi/2$ for the prolate spheroid with $b/a = 2.5$ and $2b/H = 0.8$, and for the oblate spheroid with $b/a = 0.4$ and $2b/H = 0.32$. Steady-state motion is obtained for both spheroids when $d_0/H = 0.5$ and $\beta_0 = 0, \pi/2$. The region below the lower limit of the tumbling region is for $\delta_{LW}/H < 0$, the region from which the rigid spheroid is physically excluded. Due to the definition of β, figures 19(*a*) and 19(*b*) are qualitatively mirror images of each other, in which the position with the major axis parallel to the walls is at $\beta = 0$ for the prolate spheroid and $\beta = \pi/2$ for the oblate spheroid. However, the transition from oscillating to tumbling motion occurs for smaller d_0/H for the oblate spheroid than the prolate spheroid.

3.2. *Spheroid with major axis length greater than channel height*

A particle with a major axis that is greater than the channel height can experience the four types of motion that the spheroids with major axes less than the channel height experience: (i) steady translation along x_2 without rotation; (ii) steady translation along x_2 with rotation; (iii) oscillating motion (a) in two dimensions, in which β ranges from β_0 to π-β_0 or (b) in three dimensions, in which the particle centre location, d/H, and the angles β and/or φ oscillate about their starting values with the inclination of the unique axis remaining positive for positive β_0; and (iv) tumbling motion (b) in three dimensions, in which β passes through both positive and negative values and the tip of the particle passes both above and below d/H as the particle moves along the x_2-axis. However, since this prolate spheroid's unique axis is longer than the channel spacing, it cannot experience type (iv) (a) two-dimensional tumbling. Instead, for certain initial conditions, this larger prolate spheroid can (v) become wedged between the walls of the channel in a relatively short time, despite lubrication.

3.2.1. *Prolate spheroid with $2b/H = 1.5$ and its axis of symmetry in the $x_1 = 0$ plane*

The largest prolate spheroid examined in this work has $b/a = 2.5$ and a major axis $2b/H = 1.5$, so it cannot fully rotate in the channel when aligned with its major axis in the $x_1 = 0$ plane with $\varphi = \pi/2$, precluding any type (iv) (a) two-dimensional tumbling motion in this configuration. Instead, for $\varphi = \pi/2$, this large prolate spheroid

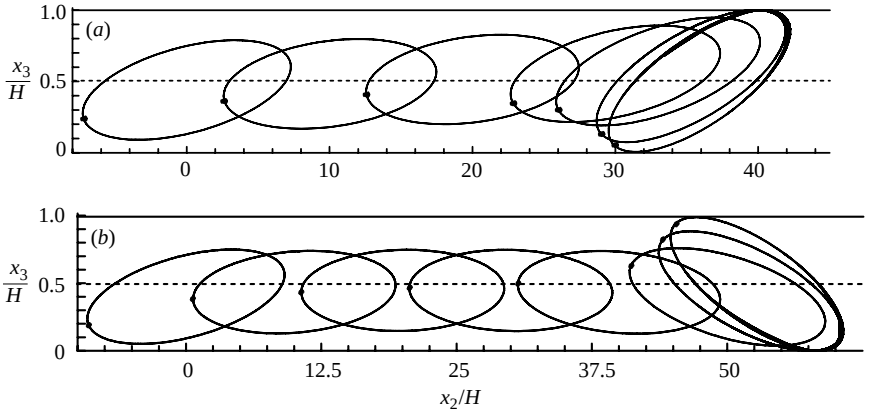

FIGURE 20. Two-dimensional projections in the $x_1 = 0$ plane for wedging of a prolate spheroid with $b/a = 2.5$ and $2b/H = 1.5$ for $\varphi = \pi/2$, $\beta_0 = \pi/12$: (*a*) $d_0/H = 0.44$, scaling of the centre location as $(x_1^c, 0.10x_2^c, x_3^c)$, and images shown at $\hat{t} = tU_c/H = 0$, 12.06, 23.75, 35.68, 39.55, 43.37 and 45.33; (*b*) $d_0/H = 0.4$, scaling of the centre location as $(x_1^c, 0.08x_2^c, x_3^c)$, and images shown at $\hat{t} = tU_c/H = 0$, 12.56, 24.47, 36.25, 48.15, 54.27, 60.85, and 64.49. The dot in each part was added to indicate particle orientation.

experiences motion of type (i), (iii) (a), and (v) described above. For $\beta = 0$ and $d_0/H = 0.5$, a steady motion of type (i) is observed. For certain cases with $\beta \neq 0$, the spheroid (v) becomes wedged in the channel, as shown by the particle projections in the $x_1 = 0$ plane in figure 20 for two selected cases of wedging with $\beta_0 = \pi/12$ and $d_0/H = 0.44$ or $d_0/H = 0.40$. For $d_0/H > 0.4$, the spheroid rotates counterclockwise (as observed along the positive x_1-axis of figure 1), passing through angles in the range $0 < \beta < \beta_{\max}$ until it wedges at $\beta_{\max}$ (figure 20*a*). ($\beta_{\max}$ is the maximum angle by physical constraints for a spheroid aligned along x_2, calculated by the formula given in § 2.5; $\beta_{\max} = 0.1977\pi$ for this spheroid.) However, for certain cases in which the spheroid's surface is initially located in close proximity to the lower wall, the increased resistance from the small gap from the lower wall causes the spheroid's major axis to rotate clockwise, passing through angles in the range $\beta < 0$ before wedging with $\beta = -\beta_{\max}$ (figure 20*b*). Figure 21 shows the change in parameters for a range of wedging cases with $\varphi = \pi/2$. The inclusion of lubrication formulae in our simulation is evident from the asymptotically shrinking gap of the spheroid from the lower wall seen in figure 21(*b*). As seen in figure 21(*d*), U_2/U_c decreases significantly as the spheroid gaps decrease.

An oscillating motion of type (iii) (a) occurs for $d_0/H < 0.41$ and $\beta_0 = 0$, as shown in figure 22. This oscillating motion probably results from the rather close proximity of the spheroid to the lower wall, which increases the drag on the spheroid and prevents it from rotating around to a wedged position. These oscillating cases replace the type (iv) (a) two-dimensional tumbling experienced by spheroids with major axes less than the channel height. The oscillations pass through a minimum at $d_0/H \approx 0.38$, where the initial direction of the spheroid's rotation changes from clockwise to counter-clockwise. For a given β_0 and initial direction of rotation (e.g. counterclockwise, which is observed for $d_0/H < 0.38$ in figure 22), the period length slightly decreases and the oscillation in β increases as d_0/H is decreased (i.e. the prolate spheroid is closer to the lower wall at the start of the simulation), due to the closer proximity of the spheroid to the lower wall.

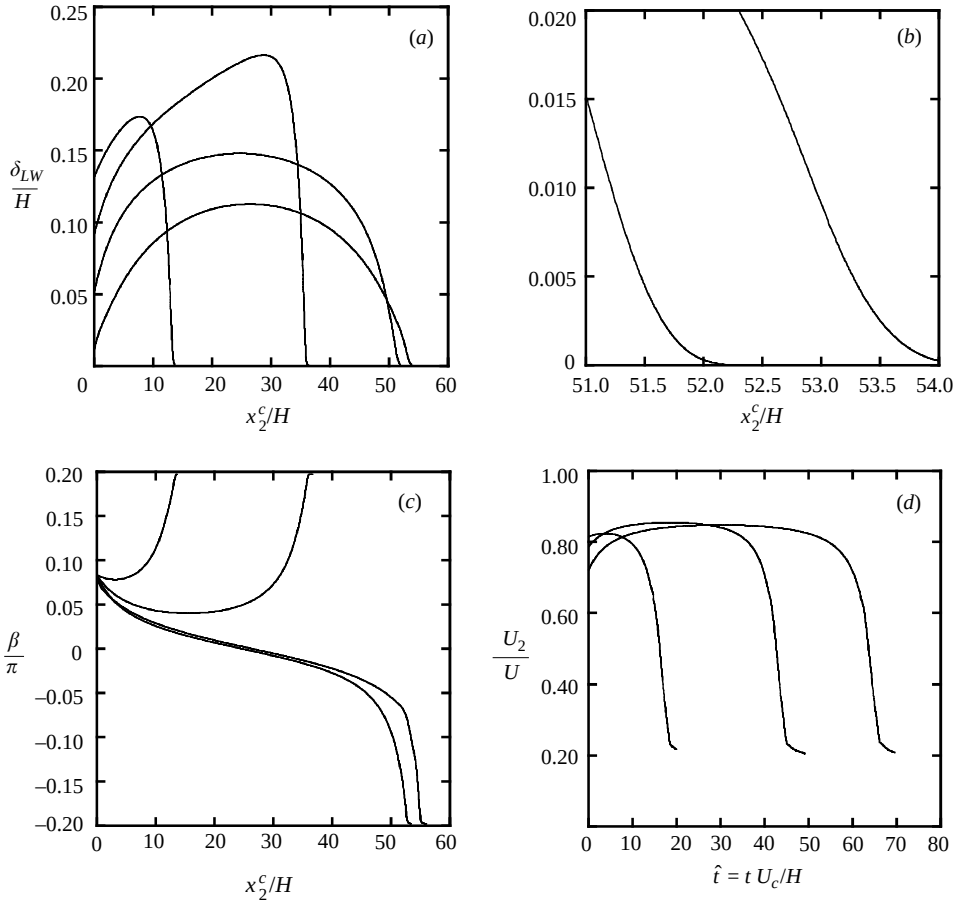

FIGURE 21. Prolate spheroid with $b/a = 2.5$ and $2b/H = 1.5$ for wedging with $\varphi = \pi/2$, $\beta_0 = \pi/12$: (*a*) δ_{LW}/H vs. x_2^c/H for $d_0/H = 0.36$, 0.40, 0.44, and 0.48 (bottom to top at $x_2^c/H = 0$), (*b*) close-up view of portion of (a) for $d_0/H = 0.36$, 0.40 (right to left), (*c*) β/π vs. x_2^c/H for $d_0/H = 0.40$, 0.36, 0.44, and 0.48 (bottom to top at $x_2^c/H = 10$), (*d*) U_2/U_c vs. $\hat{t} = tU_c/H$ for $d_0/H = 0.40$, 0.44, and 0.48 (right to left at $U_2/U_c = 0.4$).

3.2.2. *Prolate spheroid with $2b/H = 1.5$ and its axis of symmetry not confined to the $x_1 = 0$ plane*

With the additional degree of freedom given by $\varphi \neq \pi/2$, the observed motions of the prolate spheroid with $2b/H = 1.5$ are steady motions of type (i) and (ii), an oscillating motion of type (iii) (b), a tumbling motion of type (iv) (b), and wedging between the walls of type (v). As with the prolate spheroid with $2b/H = 0.8$ (§§ 3.1.1–3.1.2), steady motion of type (i) with $U_2/U_c > 0$ is observed for $d_0/H = 0.5$ and $\beta_0 = 0$ with any value of φ_0. Steady motion of type (ii) with $U_2/U_c > 0$ and $H\Omega_2'/U_c < 0$ occurs for $\varphi_0 = \beta_0 = 0$ and $0.3 < d_0/H \leqslant 0.5$. Figure 23 shows U_2/U_c and $H\Omega_2'/U_c$ for this large prolate spheroid, as well as the smaller prolate spheroid with $2b/H = 0.8$, as a function of d/H. The translational velocity decreases as the spheroid is located closer to a wall, since the smaller gap means that the spheroid is slowed more by the lower wall. As a spheroid is located closer to a wall, $|H\Omega_2'/U_c|$ experiences a maximum that is a function of the competition between greater hydrodynamic interactions, which impede the spheroid's rotation, and the larger velocity gradient

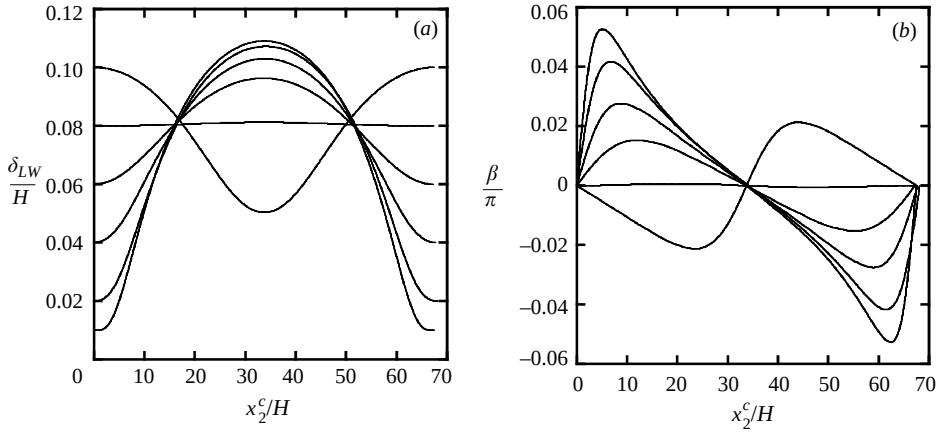

FIGURE 22. Prolate spheroid with $b/a = 2.5$ and $2b/H = 1.5$ for two-dimensional oscillating motion with $\varphi = \pi/2$, $\beta_0 = 0$, $d_0/H = 0.31$, 0.32, 0.34, 0.36, 0.38, and 0.40: (*a*) δ_{LW}/H vs. x_2^c/H (bottom to top at $x_2^c/H = 0$), (*b*) β/π vs. x_2^c/H (top to bottom at $x_2^c/H = 5$).

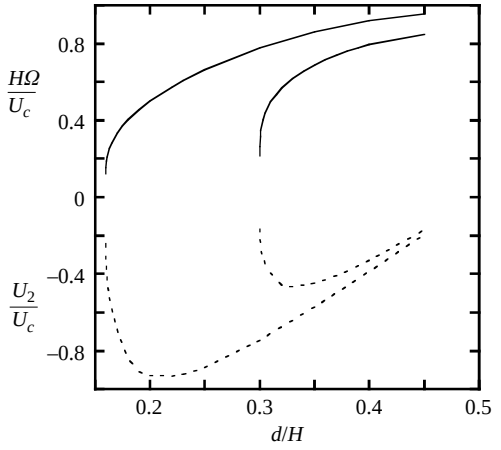

FIGURE 23. Steady-state translational and rotational velocities of prolate spheroids with $b/a = 2.5$ as a function of the centre location d/H for $\beta = \varphi = 0$, where the solid lines are for U_2/U_c and the dotted lines are for $H\Omega_2'/U_c$. For both U_2/U_c and $H\Omega_2'/U_c$, the line that extends to smaller d/H is for the prolate spheroid with $2b/H = 0.8$, while the other two lines are for the prolate spheroid with $2b/H = 1.5$.

in the Poiseuille flow, which causes rotation. A similar phenomenon regarding the maximum in rotational velocity was observed in prior boundary-integral simulation work for a sphere (Staben *et al.* 2003).

For these cases with $\varphi \neq \pi/2$, the distinction between wobbling motions (used here to describe both oscillating motions of type (iii) (b) and tumbling motions of type (iv) (b)) and wedging of type (v) is a function of φ_0, β_0, and d_0/H, such that, as d_0/H increases, the transition from wobbling to arrested motion occurs for larger β and φ. All wobbling cases pass through $\varphi = 0$, while all wedging cases do not. As was seen with the prolate spheroid with $2b/H = 0.8$, oscillating motion of type (iii) (b) and tumbling motion of type (iv) (b) are observed for $\varphi_0 \neq \pi/2$.

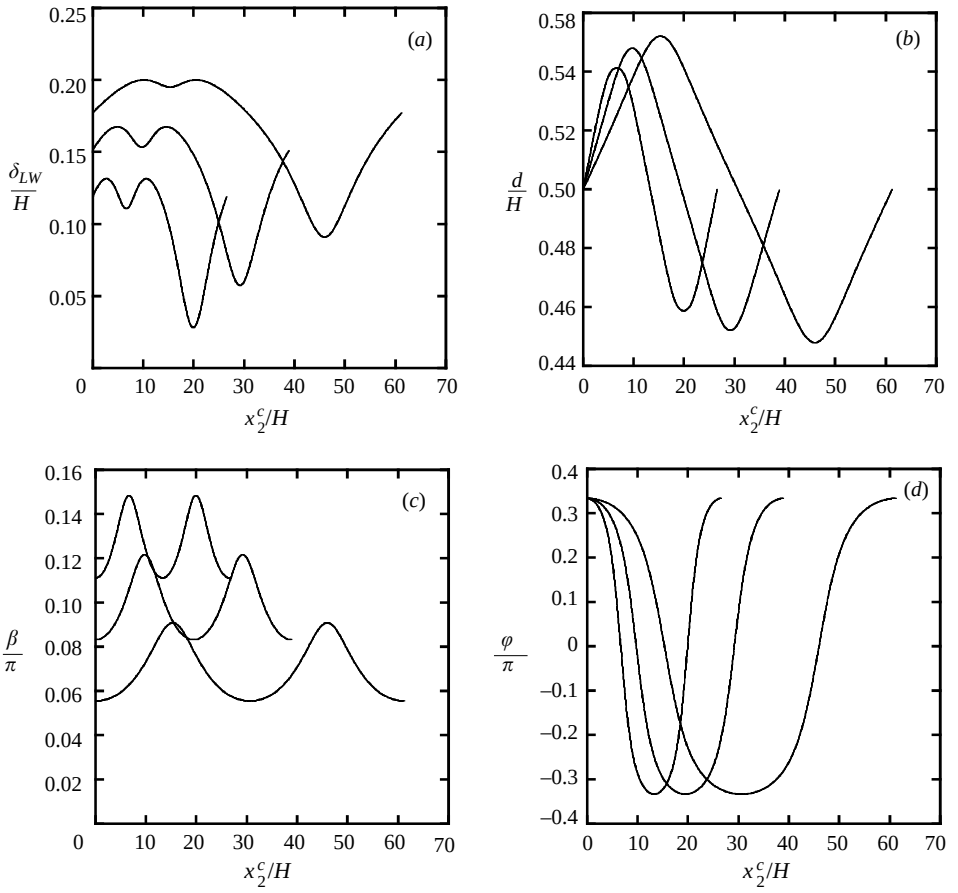

FIGURE 24. Prolate spheroid with $b/a = 2.5$ and $2b/H = 1.5$ for three-dimensional oscillating motion with $d_0/H = 0.5$, $\varphi_0 = \pi/3$, $\beta_0 = \pi/18$, $\pi/12$, and $\pi/9$: (*a*) δ_{LW}/H vs. x_2^c/H (top to bottom at $x_2^c/H = 0$), (*b*) d/H vs. x_2^c/H (right to left at minimum d/H for each curve), (*c*) β/π vs. x_2^c/H (bottom to top at $x_2^c/H = 0$), (*d*) φ/π vs. x_2^c/H (right to left at $\varphi/\pi = 0.2$ for $0 \leqslant x_2^c/H \leqslant 15$).

Figure 24 shows the variation in parameters for an oscillating motion of type (iii) (b) for $d_0/H = 0.5$ and a range of β_0, demonstrating that these oscillations exhibit the same type of symmetry about $d/H = 0.5$ as seen for the smaller prolate spheroid in § 3.1.2. A change in φ_0 (not shown for brevity) has a minor effect on the period length but a more significant effect on the maximum β and the range of d/H, where the maximum β and range of d/H increases for increasing φ_0. An increase in β_0 (figure 24) significantly decreases the period length and the range of all the parameters except φ, indicating that the range of φ is dependent mainly on the value of φ_0. As with the smaller prolate spheroid of § 3.1.1, the period length and variation in parameters (with the exception of φ) are much more significantly affected by changes in β_0 than in φ_0.

An example of type (iv) (b) tumbling motion is shown by the three-dimensional particle images of figure 25 for a case with $d_0/H = 0.4$, $\beta_0 = \pi/6$ and $\varphi_0 = 0$. This larger spheroid tumbles as it translates along the channel length, with $-\pi/6 \leqslant \beta \leqslant \pi/6$ and φ oscillating around 0. This large prolate spheroid rotates rapidly out of the

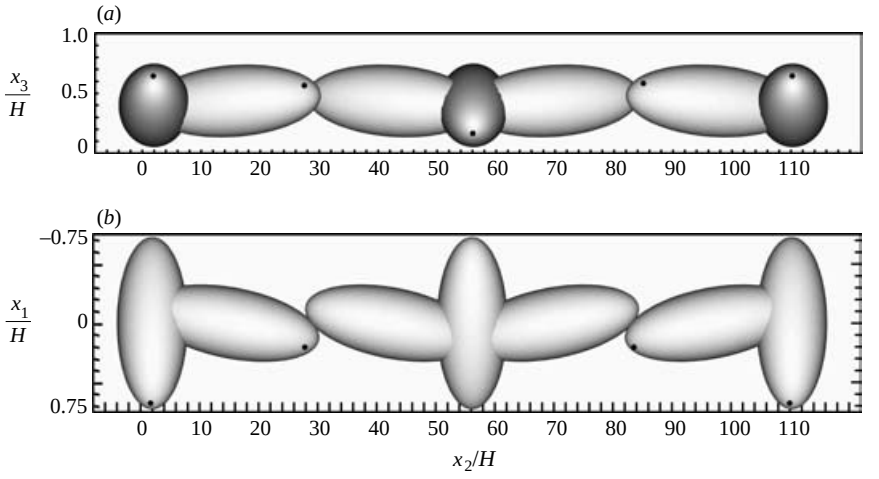

FIGURE 25. Three-dimensional images for tumbling motion of a prolate spheroid with $b/a = 2.5$ and $2b/H = 1.5$ and for $d_0/H = 0.4$, $\beta_0 = \pi/12$ and $\varphi_0 = 0$. Scaling of the centre location as $(x_1^c, 0.05x_2^c, x_3^c)$, with images at $\hat{t} = tU_c/H = 0$, 17.06, 49.13, 66.19, 83.24, 115.3, and 132.4 shown (*a*) from the side and (*b*) from the top. The dot was added to indicate particle orientation.

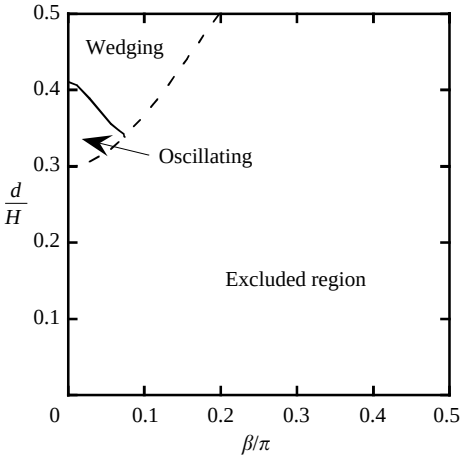

FIGURE 26. Phase-space diagram for prolate spheroid with $b/a = 2.5$ and $2b/H = 1.5$ for $\varphi = \pi/2$. The solid line demarcates the transition from oscillating motion to wedging, while the dashed line indicates the centre location for the minimum δ_{LW}/H by physical constraints. Steady motion occurs for $d_0/H = 0.5$ and $\beta_0 = 0$.

configuration with its major axis perpendicular to the undisturbed flow direction, spending most of the period in configurations with the major axis almost aligned in the Poiseuille flow direction. The three-dimensional tumbling motion can be noted by observing that the dot on the spheroid tip passes both above and below the spheroid centre during the period of motion.

3.2.3. *Demarcation of wedging and oscillating regions for axis of symmetry in the* $x_1 = 0$ *plane*

Figure 26 is the phase-space diagram demarcating the transition between type (iii) (a) two-dimensional oscillating motions and type (v) two-dimensional wedging

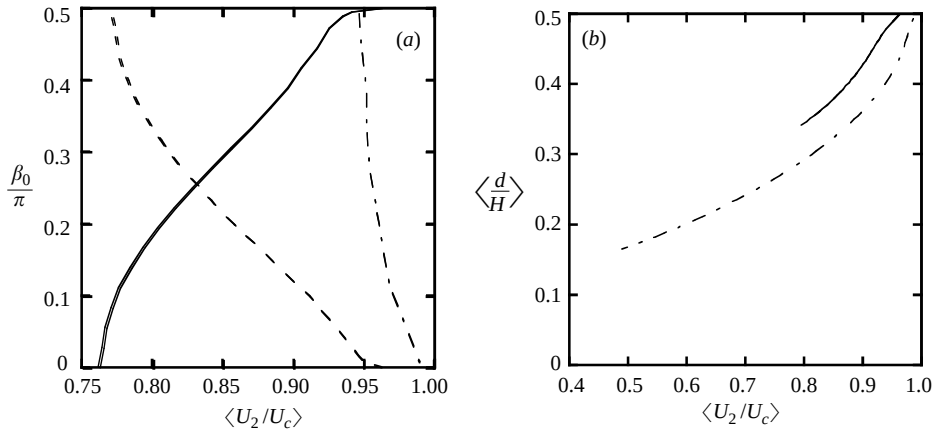

FIGURE 27. Average velocity along the channel length for prolate and oblate spheroids: (*a*) $\langle U_2/U_c \rangle$ vs. B_0/π for two-dimensional oscillating motion with $\varphi = \pi/2$, for prolate spheroid with $b/a = 2.5$ and $2b/H = 0.4$ (dot-dash line) or 0.8 (dashed line), and oblate spheroid with $b/a = 0.4$ and $2b/H = 0.32$ (solid line), (*b*) $\langle U_2/U_c \rangle$ vs. $\langle d/H \rangle$ for two-dimensional tumbling motion with $\varphi = \pi/2$, for prolate spheroid with $b/a = 2.5$ and $2b/H = 0.4$ (dot-dash line) or 0.8 (dotted line, overlaps solid line), and oblate spheroid with $b/a = 0.4$ and $2b/H = 0.32$ (solid line).

of the spheroid between the walls for $\varphi = \pi/2$. For this large spheroid, only locations near the wall yield two-dimensional oscillating motion, since the interaction with the nearby wall prevents the spheroid from rotating around to wedge in the channel. The spheroid becomes wedged between the walls for locations in or near the midplane of the channel, since, for these configurations, the large particle has a lift velocity ($U_3/U_c \neq 0$) that leads to wedging. The excluded region for this large particle is a much larger portion of the parameter space (figure 26) than for the smaller oblate and prolate spheroids (figure 19).

3.3. *Average particle velocities*

A result of interest for various applications is the average particle velocity as a function of particle size and initial conditions. Average particle velocities were calculated for spheroids with their unique axis confined to the $x_1 = 0$ plane ($\varphi = \pi/2$). The three spheroids examined in figure 27 are two prolate spheroids with $b/a = 2.5$ and $2b/H = 0.4$ or 0.8, respectively, and one oblate spheroid with $b/a = 0.4$ and $2b/H = 0.32$. Type (iii) (a) oscillating motions and type (iv) (a) tumbling motions are separated into two figures.

Figure 27(*a*) presents the average particle velocity along the primary flow direction, $\langle U_2/U_c \rangle$, for $d_0/H = 0.5$ as a function of β_0/π for the type (iii) (a) two-dimensional oscillating motion with $\varphi = \pi/2$ for three spheroids with major axes less than the channel height. For these spheroids with their unique axes confined to the $x_1 = 0$ plane, the oscillating motion occurs for centre locations in or near the midplane of the channel, with each trajectory passing through a unique combination of $d_0/H = 0.5$ and β_0. For each of these three spheroids, the average particle velocity decreases with an increase in the initial inclination angle of the major axis in the $x_1 = 0$ plane, due to the increased interactions with the walls of the channel that occur for these steeper angles. $\langle U_2/U_c \rangle$ for a given β_0 decreases as the particle's major axis length and volume increase, such that $\langle U_2/U_c \rangle$ is lowest for the oblate spheroid with two dimensionless axes $2a/H = 2c/H = 0.8$ and highest for the prolate spheroid with

a single dimensionless major axis $2b/H = 0.4$. The increased volume of the oblate spheroid decreases its velocity only slightly compared to the prolate spheroid with the same major axis length for a given configuration. The curve for the oblate spheroid is qualitatively a mirror image of that for the prolate spheroid of the same major axis length, since β is defined as the angle of the unique axis with respect to the $x_3 = 0$ plane.

Figure 27(*b*) presents $\langle U_2/U_c \rangle$ versus $\langle d/H \rangle$ for the type (iv) (a) two-dimensional tumbling motion with $\varphi = \pi/2$ for the three spheroids with their major axes less than the channel height. Each point was obtained using a unique combination of $\beta_0 = 0$ (for prolate spheroids) or $\beta_0 = \pi/2$ (for oblate spheroids) and d_0/H. For the two spheroids with dimensionless major axis lengths of 0.8, $0.345 \leqslant d_0/H \leqslant 0.5$, while for the small prolate spheroid, $0.16 \leqslant d_0/H \leqslant 0.5$, with each range chosen to ensure that $\delta_{LW}/H > 1 \times 10^{-4}$ for the entire simulation. For each spheroid, $\langle U_2/U_c \rangle$ decreases with decreasing $\langle d/H \rangle$, since the interaction of the spheroid with the lower wall increases with a decrease in the centre location. For the two prolate spheroids at a given average centre location, the smaller spheroid ($2b/H = 0.4$) has significantly less volume and its surface is farther from the lower wall than the larger spheroid ($2b/H = 0.8$), which increases its velocity over that of the larger spheroid at the same $\langle d/H \rangle$. The increased volume of the oblate spheroid has a minimal effect upon $\langle U_2/U_c \rangle$ compared with the prolate spheroid of the same major axis length, as evidenced by the overlapping $\langle U_2/U_c \rangle$ curves for these two spheroids. A comparison between figures 8 and 14, which show type (iv) (a) two-dimensional tumbling trajectories for a range of d_0/H for each particle, supports this finding. The oblate spheroid spends a longer portion of the period in the configuration with its major axes parallel to the walls ($\beta \approx -\pi/2$ in figure 14*b*) than the prolate spheroid does ($\beta \approx -\pi$ in figure 8*b*), which minimizes the effects of the increased volume and surface area of the oblate spheroid compared to the prolate spheroid. The reduction in $\langle d/H \rangle$ for a given $\langle U_2/U_c \rangle$ value does mean that the $\langle U_2/U_c \rangle$ curve for the oblate spheroid runs to lower $\langle d/H \rangle$ for the range of d_0/H used.

4. Concluding remarks

We have applied a novel boundary-integral algorithm (Staben *et al.* 2003) to analyse the motion of neutrally buoyant three-dimensional spheroids in low-Reynolds-number Poiseuille flow between parallel plates. As with our prior work for a sphere (Staben *et al.* 2003), our solution uses the Stokeslet between two plane walls in the kernel of the boundary-integral equation (2.4). The boundary integrals are solved in the mobility formulation and numerically inverted to obtain the resistance formulation. Singularities in the resistance coefficients that occur for near-contact motion are subtracted off using asymptotic formulae (Cox 1974; Claeys & Brady 1989). The resulting Δ-coefficients, along with other non-zero but non-singular resistance coefficients and Poiseuille flow coefficients, are tabulated and used in a three-dimensional dynamic simulation of spheroid motion in a Poiseuille flow between two parallel plates. Use of adaptive meshing in the boundary-integral solutions and use of the asymptotic formulae to obtain Δ-coefficients for tabulation allow accurate calculations for approach to infinitesimally small spacing from the bounding walls of the system.

Results are separated into two ranges: spheroids with major axes less than the channel height, and spheroids with longer axes. Spheroids with major axes less than the channel height experience steady-state motion with $U_2/U_c \neq 0$ only for

configurations on the midplane of the channel with any value of φ and $\beta = 0$ for prolate spheroids or $\beta = \pi/2$ for oblate spheroids. For initial centre locations in or near the midplane with $\varphi = \pi/2$, these spheroids experience two-dimensional oscillations about $d/H = 0.5$. A two-dimensional tumbling motion occurs for $\varphi = \pi/2$ and certain combinations of d_0/H and β_0, with the requirement that trajectories with $d_0/H \neq 0.5$ for prolate spheroids containing $\beta = 0$ or for oblate spheroids containing $\beta = \pi/2$ are always tumbling trajectories. The distinction between oscillating and tumbling motion for $\varphi = \pi/2$ occurs for smaller d_0/H for an oblate spheroid compared to a prolate spheroid of the same cross-section. Allowing $\varphi \neq \pi/2$ yields three-dimensional oscillating motions for centre locations in or near the midplane of the channel and three-dimensional tumbling motions for centre locations closer to a wall. For both two-dimensional and three-dimensional motions, the period length of tumbling motions decreases for a decrease in d_0/H, while the period length of oscillating motions decreases for an increase in the inclination of the spheroid's major axis with respect to the walls.

A spheroid with its major axis greater than the channel height is unable to fully rotate in the channel to experience two-dimensional tumbling when $\varphi = \pi/2$, and, instead, experiences either a two-dimensional oscillating motion for initial centre locations near the walls (the equivalent of two-dimensional tumbling for spheroids with major axes less than the channel height) or becomes wedged between the walls for initial centre locations in or near the midplane of the channel. The inclusion of lubrication asymptotics in our work is evidenced by the asymptotically shrinking gaps from the walls observed for cases in which the large prolate spheroid becomes wedged between the walls. As with the smaller spheroids, this large prolate spheroid experiences three-dimensional tumbling and oscillating motions for configurations in which the unique axis is not confined to a plane parallel to the flow direction and perpendicular to the walls, with oscillating motions near the midplane and tumbling motions closer to a wall.

The average particle velocity as a function of particle centre location with $\varphi = \pi/2$ is highly dependent upon the type of motion experienced and the initial configuration of the problem. The average particle velocity for two-dimensional motions of spheroids with their major axes less than the channel height can be separated into tumbling or oscillating motions. For the two-dimensional oscillating motion, the average particle velocity decreases with an increase in the inclination angle of the major axis in the $x_1 = 0$ plane, since a larger inclination angle means a greater interaction with the bounding walls of the system. For the two-dimensional tumbling motion, the average particle velocity decreases for a decrease in $\langle d/H \rangle$ since, for these locations, the particle spends more time in close proximity to the lower wall of the system. The larger the spheroid is in either axis length or volume, the lower the average velocity is for a given centre location, although the increase in volume has only a minor effect. These average particle velocity results can be used to optimize particle transport of spheroidal particles in a Poiseuille flow between two parallel plates, as might be encountered in various applications, e.g. microfluidics.

This work was supported by the SIMBIOSYS program of the Defense Advanced Research Projects Agency. M.E.S. was also supported by a National Science Foundation Graduate Research Fellowship, a NASA Graduate Student Researchers' Program fellowship, and the U.S. Department of Education's Graduate Assistantships in Areas of National Need program. We also appreciate the referee's suggestion for

comparison of our results with Jeffery's (1922) solution for an isolated spheroid in a shear flow.

Appendix A. Derivation of the CB ellipsoid asymptotic formulae

In reducing the asymptotic formulae developed by Claeys & Brady (1989) for $F_3^{r_1}$, $F_3^{t_2}$ $T_1^{t_3}$, $F_2^{t_3}$ and the second-order correction to $F_3^{t_3}$, we found that $\tilde{p}_h$ (the first-order correction to the pressure field) in their equation (2.17) should have the opposite sign to that shown in their work. The correct form of their (2.17), as used in the derivation of $F_3^{r_1}$ (2.12*b*), $F_3^{t_2}$ (2.15*b*), $T_1^{t_3}$ (2.16*a*) and $F_2^{t_3}$ (2.16*b*), is

$$\tilde{p}_h = \frac{-6U_3}{\lambda_1+\lambda_2}\left\{\sum_{i=0}^{3}\kappa_i\cos^{3-i}\theta\sin^i\theta\ \frac{\hat{r}^3}{(1+\hat{r}^2)^3}\right.$$
$$\left.+\left[\frac{3\lambda_2\kappa_3+\lambda_1\kappa_1}{2\lambda_1+3\lambda_2}\ \sin\theta+\frac{3\lambda_1\kappa_0+\lambda_2\kappa_2}{3\lambda_1+2\lambda_2}\ \cos\theta\right]\ \frac{\hat{r}}{(1+\hat{r}^2)^2}\right\}, \quad (A\,1)$$

for our case of a stationary wall as one of the surfaces ($U_3'=0$ in their notation). The elliptic coordinates $(\hat{r},\hat{\theta})$, are related to $(\hat{x}_1,\hat{x}_2)$, by the expressions $\hat{x}_1=\tilde{x}_1=\overline{x}_1=\hat{r}\cos\theta/\sqrt{\lambda_1}$ and $\hat{x}_2=\tilde{x}_2=\overline{x}_2=\hat{r}\cos\theta/\sqrt{\lambda_2}$. The symbols λ_1, λ_2, are defined in § 2.5 of the present paper, and the remaining variables are as defined by Claeys & Brady (1989). Unfortunately, the sign error in $\tilde{p}_h$ in Claeys & Brady (1989) was propagated through the subsequent equations for $F_3^{r_1}$, $F_3^{t_2}$, $T_1^{t_3}$, and $F_2^{t_3}$ in their paper. Starting from the correct equation (A 1) for $\tilde{p}_h$ above, we rederived the expressions for these four resistance coefficients for our specific case of an ellipsoid near a plane wall. The equations for the higher-order terms of the velocity field that use $\tilde{p}_h$, given as equations (2.18*a–c*) in Claeys & Brady (1989), are

$$\tilde{u}_{h1}=\frac{1}{2}\left[\frac{\partial\tilde{p}_h}{\partial\overline{x}_1}\,\overline{x}_3^2-\left(\frac{\partial\tilde{p}_z}{\partial\overline{x}_1}\,h_h+\frac{\partial\tilde{p}_h}{\partial\overline{x}_1}\,h_z\right)\overline{x}_3\right], \quad (A\,2)$$

$$\tilde{u}_{h2}=\frac{1}{2}\left[\frac{\partial\tilde{p}_h}{\partial\overline{x}_2}\,\overline{x}_3^2-\left(\frac{\partial\tilde{p}_z}{\partial\overline{x}_2}\,h_h+\frac{\partial\tilde{p}_h}{\partial\overline{x}_2}\,h_z\right)\overline{x}_3\right], \quad (A\,3)$$

$$\begin{aligned}\tilde{u}_{h3}=&-\frac{1}{6}\overline{\nabla}^2\tilde{p}_h\overline{x}_3^3+\frac{1}{4}\left(h_h\overline{\nabla}^2\tilde{p}_z+\overline{\nabla}\tilde{p}_z\cdot\overline{\nabla}h_h+h_z\overline{\nabla}^2\tilde{p}_h+\overline{\nabla}\tilde{p}_h\cdot\overline{\nabla}h_z\right)\overline{x}_3^2\\&-\frac{1}{2}\,\frac{\overline{x}_1}{R_1}\left(\frac{\partial\tilde{p}_h}{\partial\overline{x}_1}\,\overline{x}_3^2-\frac{\partial\tilde{p}_z}{\partial\overline{x}_1}\,h_h\overline{x}_3-\frac{\partial\tilde{p}_h}{\partial\overline{x}_1}\,h_z\overline{x}_3\right)\\&-\frac{1}{2}\,\frac{\overline{x}_2}{R_2}\left(\frac{\partial\tilde{p}_h}{\partial\overline{x}_2}\,\overline{x}_3^2-\frac{\partial\tilde{p}_z}{\partial\overline{x}_2}\,h_h\overline{x}_3-\frac{\partial\tilde{p}_h}{\partial\overline{x}_2}\,h_z\overline{x}_3\right)\\&-\frac{1}{2}\sum_{i=0}^{2}(3-i)\Gamma_i\overline{x}_1^{2-i}\overline{x}_2^i\left(\frac{\partial\tilde{p}_z}{\partial\overline{x}_1}\overline{x}_3^2-\frac{\partial\tilde{p}_z}{\partial\overline{x}_1}h_z\overline{x}_3\right)\\&-\frac{1}{2}\sum_{i=1}^{3}i\,\Gamma_i\overline{x}_1^{3-i}\overline{x}_2^{i-1}\left(\frac{\partial\tilde{p}_z}{\partial\overline{x}_2}\overline{x}_3^2-\frac{\partial\tilde{p}_z}{\partial\overline{x}_2}h_z\overline{x}_3\right), \quad (A\,4)\end{aligned}$$

where, for the present work, $\overline{x}_1=x_1$, $\overline{x}_2=x_2$, $\overline{x}_3=x_3$, $h_z=1+\lambda_1x_1^2+\lambda_2x_2^2$, and $\tilde{p}_h$ is as defined in (A 1); κ_1, κ_3, Γ_1, and Γ_3 are given in § 2.5 of the present work; and the rest of the variables are as defined in Claeys & Brady (1989). For our problem, $\chi=0$ in equation (2.6) of Claeys & Brady (1989), as well as $\kappa_0=\kappa_2=0$. Here, we show some

of the intermediate steps in our derivation of $F_2^{t_3}$ to demonstrate the methodology we used.

To find $F_2^{t_3}$, we start from equation (1.22*b*) of Claeys & Brady (1989),

$$F_2 = -\int_S \boldsymbol{e}_2 \cdot \boldsymbol{\sigma} \cdot \mathrm{d}S = \epsilon^{k-1/2} \int_S \left(\frac{\tilde{x}_2}{R_2}\ \tilde{p}_z - \frac{\partial \tilde{u}_{z2}}{\partial \tilde{x}_3} \right) \mathrm{d}\tilde{x}_1\, \mathrm{d}\tilde{x}_2 + \epsilon^k \int_S \left(\frac{\tilde{x}_2}{R_2}\ \tilde{p}_h - \frac{\partial \tilde{u}_{h2}}{\partial \tilde{x}_3} + \sum_{i=1}^{3} i\, \Gamma_i \tilde{x}_1^{3-i} \tilde{x}_2^{i-1} \tilde{p}_z \right) \mathrm{d}\tilde{x}_1\, \mathrm{d}\tilde{x}_2, \quad \text{(A 5)}$$

where F_2 is the second component of the force exerted by the surface S on the surrounding fluid and ϵ is the non-dimensional gap as defined in Claeys & Brady (1989), with $k = 0$. With introduction of the elliptic coordinates described above, the $\epsilon^{k-1/2}$ term of (A 5) has $\cos\theta$-dependence, which makes this term zero after integration in θ. Equation (A 5) becomes

$$F_2 = \int_S \left(\frac{\tilde{x}_2}{R_2}\ \tilde{p}_h - \frac{\partial \tilde{u}_{h2}}{\partial \tilde{x}_3} + \sum_{i=1}^{3} i\, \Gamma_i \tilde{x}_1^{3-i} \tilde{x}_2^{i-1} \tilde{p}_z \right) \frac{\hat{r}}{\sqrt{\lambda_1 \lambda_2}}\ \mathrm{d}\hat{r}\, \mathrm{d}\theta. \quad \text{(A 6)}$$

From here, we must express the terms in equation (A 6) in λ_1, λ_2, $\hat{r}$, $\hat{\theta}$, and other parameters prior to integration in $\hat{r}$ and $\hat{\theta}$.

The leading-order term of the pressure, $\tilde{p}_z$, is (equation (2.9) of Claeys & Brady 1989)

$$\tilde{p}_z = \frac{3U_3}{\lambda_1 + \lambda_2}\ \frac{1}{(1+\hat{r}^2)^2}, \quad \text{(A 7)}$$

for our case of a stationary wall. Since it is the $r \to \infty$ behaviour that contributes to the log-terms of $F_2^{t_3}$, simplifications can be made, such as $(1+\hat{r}^2)^2 \approx \hat{r}^4$ to yield

$$\tilde{p}_z \approx \frac{3U_3}{\lambda_1 + \lambda_2}\ \frac{1}{\hat{r}^4}. \quad \text{(A 8)}$$

The first term on the right-hand side of (A 6), $\tilde{x}_2 \tilde{p}_h / R_2$, is explicitly represented as a combination of $\tilde{x}_2$ expressed in elliptic coordinates and equation (A 1) for $\tilde{p}_h$, to give

$$\frac{\tilde{x}_2}{R_2}\ \tilde{p}_h = \frac{-6U_3 \sin\theta}{R_2 \sqrt{\lambda_2}(\lambda_1 + \lambda_2)}\ \frac{1}{\hat{r}^2} \left\{ \sum_{i=0}^{3} \kappa_i \cos^{3-i}\theta \sin^i\theta + \left[\frac{3\lambda_2\kappa_3 + \lambda_1\kappa_1}{2\lambda_1 + 3\lambda_2}\ \sin\theta \right] \right\}, \quad \text{(A 9)}$$

with $\kappa_0 = \kappa_2 = 0$. Some intermediate calculations for the next term of (A 6), $\partial \tilde{u}_{h2}/\partial \tilde{x}_3$, include

$$\left. \frac{\partial \tilde{u}_{h2}}{\partial \overline{x}_3} \right|_{\overline{x}_3 = 0} = -\frac{h_h}{2}\ \frac{\partial \tilde{p}_z}{\partial \overline{x}_2} - \frac{h_z}{2}\ \frac{\partial \tilde{p}_h}{\partial \overline{x}_2}, \quad \text{(A 10)}$$

where the differentiation is performed at the particle surface, $\overline{x}_3 = 0$. Differentiation of the two terms on the right-hand side of (A 10) yields

$$\frac{\partial \tilde{p}_z}{\partial \overline{x}_2} = -\frac{12U_3}{\lambda_1 + \lambda_2}\ \frac{\sqrt{\lambda_2}\sin\theta}{\hat{r}^5} \quad \text{(A 11)}$$

and

$$\frac{\partial \tilde{p}_h}{\partial \overline{x}_2} = \frac{\partial \tilde{p}_h}{\partial \hat{r}}\ \frac{\partial \hat{r}}{\partial \overline{x}_2} + \frac{\partial \tilde{p}_h}{\partial \theta}\ \frac{\partial \theta}{\partial \overline{x}_2} \quad \text{(A 12)}$$

which gives

$$\left.\frac{\partial \tilde{u}_{h2}}{\partial \bar{x}_3}\right|_{\bar{x}_3=0} = \frac{6U_3\sqrt{\lambda_2}\sin\theta}{\lambda_1+\lambda_2}\ \frac{1}{\hat{r}^2}\sum_{i=0}^{3}\kappa_i\cos^{3-i}\theta\sin^i\theta - \frac{9U_3\sqrt{\lambda_2}\sin\theta}{\lambda_1+\lambda_2}\ \frac{1}{\hat{r}^2}\ A + \frac{3U_3\sqrt{\lambda_2}\cos\theta}{\lambda_1+\lambda_2}\ \frac{1}{\hat{r}^2}\ \frac{\partial A}{\partial\theta}, \quad \text{(A 13)}$$

where

$$A = \sum_{i=0}^{3}\kappa_i\cos^{3-i}\theta\sin^i\theta + \left(\frac{3\lambda_2\kappa_3+\lambda_1\kappa_1}{2\lambda_1+3\lambda_2}\ \sin\theta\right). \quad \text{(A 14)}$$

The last term of (A 6) is represented as

$$\sum_{i=1}^{3} i\,\Gamma_i\tilde{x}_1^{3-i}\tilde{x}_2^{i-1}\tilde{p}_z = \frac{3U_3}{\lambda_1+\lambda_2}\ \frac{1}{\hat{r}^2}\sum_{i=1}^{3} i\,\Gamma_i\left(\frac{\cos\theta}{\sqrt{\lambda_1}}\right)^{3-i}\left(\frac{\sin\theta}{\sqrt{\lambda_2}}\right)^{i-1}. \quad \text{(A 15)}$$

Equations (A 9), (A 13), and (A 15) are substituted into (A 6) and simplifications are made by combining terms. The integration in $\hat{r}$ is performed up to $\hat{r}_0$, where the value of $\hat{r}_0$ lies in the overlap region of the inner and outer solutions. The logarithmic divergence of the integral at $\hat{r}_0 \to \infty$ is handled by noting that $\ln\hat{r}_0 = -\frac{1}{2}\ln\epsilon + \ln(\hat{r}_0\epsilon^{1/2})$. The second-term contribution vanishes when the outer solution is taken into account, making the results independent of the cut-off radius $\hat{r}_0$. Thus, following more simplifications, the formula for $F_2^{t_3}$ (2.16*b*) is obtained. Since $F_2^{t_3} = F_3^{t_2}$, this derivation holds for $F_3^{t_2}$ (2.15*b*). The formula for $T_1^{t_3}$ starts from equation (1.23*a*) of Claeys & rady (1989),

$$T_1 = \epsilon^{k-1/2}\int_S \tilde{x}_2\tilde{p}_z\,\mathrm{d}\tilde{x}_1\,\mathrm{d}\tilde{x}_2 + \epsilon^k\int_S \tilde{x}_2\tilde{p}_h\,\mathrm{d}\tilde{x}_1\,\mathrm{d}\tilde{x}_2. \quad \text{(A 16)}$$

As with the formula for $F_2^{t_3}$, substitution of the elliptic coordinates and subsequent θ-dependence makes the $\epsilon^{k-1/2}$ term zero. The second term is equivalent to the first term of (A 6) without R_2^{-1}, and, as such, has already been shown in (A 9). Integration of (A 16) with these modifications yields (2.16*a*), which is equivalent to (2.12*b*) for $F_3^{r_1}$.

The sign error in $\tilde{p}_h$ has also affected the expression for the $O(\ln\delta)$-term of $F_3^{t_3}$, but a formidable algebraic effort would be needed to derive this term. To avoid this difficulty, we pursued an alternate method (briefly described in § 2.5) to obtain this correction from one-wall boundary-integral calculations.

Appendix B. Transformation of asymptotic formulae from surface point to centre point

The one-wall asymptotic formulae (2.12)–(2.16) assume that the particle kinematics and hydrodynamic response are described with respect to the point on the particle surface nearest the wall. To use the asymptotic formulae in two-wall calculations, which generally have two lubrication regions from the two walls of the channel, these formulae must necessarily be transformed from the surface point(s) to the particle centre. For an asymptotic formula involving rotation (e.g. any formula with r_i as the superscript, for rotation about the ith axis), the formula for rotation applied at the surface point must be converted to torques and forces about the same point for a rotation applied at the centre. Pure rotation about the centre is a superposition of

the pure rotation about the surface point o and a pure translation with the velocity $\boldsymbol{U}^o = \boldsymbol{\Omega} \times (\boldsymbol{x}^o - \boldsymbol{x}^c)$. Accordingly, the forces ($\boldsymbol{F}$) and torques ($\boldsymbol{T}_0$) from one wall due to pure rotation about the particle centre can be written as

$$F_k = \Omega_j F_k^{r_j} + U_j^o F_k^{t_j} \tag{B1}$$

for force F, or

$$(T_k)_o = \Omega_j T_k^{r_j} + U_j^o T_k^{t_j} \tag{B2}$$

for torque T, respectively, where the coefficients have been introduced in (2.12)–(2.16) and the torques (B2) are still calculated about the surface point o. These torques (B2) must be further converted to those about the particle centre

$$(\boldsymbol{T})_c = \int_S [(\boldsymbol{x} - \boldsymbol{x}_c) \times \boldsymbol{\sigma}_n] dS = (\boldsymbol{T})_o + (\boldsymbol{x}_o - \boldsymbol{x}_c) \times \boldsymbol{F}. \tag{B3}$$

As a result, the one-wall singular contributions to the forces due to pure rotation about the centre with $\boldsymbol{\Omega} = (1, 0, 0)$ take the form

$$\left(F_2^{r_1}\right)_c = \left(F_{2,Cox}^{r_1}\right)_o + y^* F_{2,CB}^{t_3} - (z^* - z^c) F_{2,Cox}^{t_2}, \tag{B4}$$

$$\left(F_3^{r_1}\right)_c = \left(F_{3,CB}^{r_1}\right)_o + y^* \left(F_{3,Cox}^{t_3} + mb \ln(\delta)\right) - (z^* - z^c) F_{3,CB}^{t_2}. \tag{B5}$$

Other coefficients are handled in a similar manner to obtain

$$\left(F_1^{r_2}\right)_c = \left(F_{1,Cox}^{r_2}\right)_o - (z^* - z^c) F_{1,Cox}^{t_1}, \tag{B6}$$

$$\left(T_1^{t_2}\right)_c = \left(T_{1,Cox}^{t_2}\right)_o + y^* F_{3,CB}^{t_2} - (z^* - z^c) F_{2,Cox}^{t_2}, \tag{B7}$$

$$\left(T_1^{t_3}\right)_c = \left(T_{1,CB}^{t_3}\right)_o + y^* \left(F_{3,Cox}^{t_3} + mb \ln(\delta)\right) - (z^* - z^c) F_{2,CB}^{t_3}, \tag{B8}$$

$$\left(T_1^{r_1}\right)_o = \left(T_{1,Cox}^{r_1}\right)_o + y^* \left(T_{1,CB}^{t_3}\right)_o - (z^* - z^c) \left(T_{1,Cox}^{t_2}\right)_o, \tag{B9}$$

$$\left(T_2^{r_2}\right)_o = \left(T_{2,Cox}^{r_2}\right)_o + (z^* - z^c) \left(T_{2,Cox}^{t_1}\right)_o. \tag{B10}$$

Torque coefficients at the surface (due to rotation) must then be transformed to a torque at the centre:

$$\left(T_1^{r_1}\right)_c = \left(T_1^{r_1}\right)_o + y^* \left(F_3^{r_1}\right)_c - (z^* - z^c) \left(F_2^{r_1}\right)_c, \tag{B11}$$

$$\left(T_2^{r_2}\right)_c = \left(T_2^{r_2}\right)_o + (z^* - z^c) \left(F_1^{r_2}\right)_c. \tag{B12}$$

These formulae (B4)–(B12), as well as the untransformed formulae ($F_{1,Cox}^{t_1}$, $F_{2,Cox}^{t_2}$, $F_{3,CB}^{t_2}$, $F_{2,CB}^{t_3}$, and $F_{3,Cox}^{t_3}$) are to form Δ-coefficients during tabulation and in adding the lubrication contributions back in dynamic simulations.

REFERENCES

Beebe, D. J., Mensing, G. A. & Walker, G. M. 2002 Physics and applications of microfluidics in biology. *Annu. Rev. Biomed. Engng* **4**, 261–286.

Blake, J. R. 1971 A note on the image system for a Stokeslet in a no-slip boundary. *Proc. Camb. Phil. Soc. – Math. Phys. Sci.* **70**, 303–310.

Brenner, H. & Bungay, P. M. 1971 Rigid-particle and liquid-droplet models of red cell motion in capillary tubes. *Federation Proc.* **30**, 1565–1576.

Chen, C. C., Zappe, S., Sahin, O., Zhang, X. J., Fish, M., Scott, M. & Solgaard, O. 2004 Design and operation of a microfluidic sorter for *Drosophila* embryos. *Sens. Actuator B-Chem.* **102**, 59–66.

Claeys, I. L. & Brady, J. F. 1989 Lubrication singularities of the grand resistance tensor for 2 arbitrary particles. *Physicochem. Hydrodyn.* **11**, 261–293.

Cox, R. G. 1974 The motion of suspended particles almost in contact. *Intl J. Multiphase Flow* **1**, 343–371.

Cristini, V., Blawzdziewicz, J. & Loewenberg, M. 2001 An adaptive mesh algorithm for evolving surfaces: simulations of drop breakup and coalescence. *J. Comput. Phys.* **168**, 445–463.

El-Kareh, A. W. & Secomb, T. W. 2000 A model for red blood cell motion in bifurcating microvessels. *Intl J. Multiphase Flow* **26**, 1545–1564.

Fletcher, R. 1976 *Conjugate Gradient Methods for Indefinite Systems.* Lecture Notes in Mathematics, vol. 506. Springer.

Ganatos, P., Pfeffer, R. & Weinbaum, S. 1980*a* A strong interaction theory for the creeping motion of a sphere between plane parallel boundaries. Part 2. Parallel motion. *J. Fluid Mech.* **99**, 755–783.

Ganatos, P.,Weinbaum, S. & Pfeffer, R. 1980*b* A strong interaction theory for the creeping motion of a sphere between plane parallel boundaries. Part 1. Perpendicular motion. *J. Fluid Mech.* **99**, 739–753.

Ganatos, P., Weinbaum, S. & Pfeffer, R. 1982 Gravitational and zero-drag motion of a sphere of arbitrary size in an inclined channel at low Reynolds-number. *J. Fluid Mech.* **124**, 27–43.

Goldman, A. J., Cox, R. G. & Brenner, H. 1967*a* Slow viscous motion of a sphere parallel to a plane wall. I. Motion through a quiescent fluid. *Chem. Engng Sci.* **22**, 637–651.

Goldman, A. J., Cox, R. G. & Brenner, H. 1967*b* Slow viscous motion of a sphere parallel to a plane wall. II. Couette flow. *Chem. Engng Sci.* **22**, 653–660.

Griggs, A. J., Zinchenko, A. Z. & Davis, R. H. 2006 Low-Reynolds-number motion of a deformable droplet between two parallel walls. *Intl J. Multiphase Flow* (submitted).

Happel, J. & Brenner, H. 1986 *Low Reynolds Number Hydrodynamics.* Martinus Nijhoff.

Hebeker, F.-K. 1986 Efficient boundary element methods for three-dimensional exterior viscous flow. *Numer. Meth. PDE* **2**, 273–297.

Jeffery, G. B. 1922 The motion of ellipsoidal particles immersed in a viscous fluid. *Proc. R. Lond. Ser.* A **102**, 161–179.

Kim, S. & Karrila, S. J. 1991 *Microhydrodynamics: Principles and Selected Applications.* Butterworth-Heinemann.

Li, P. C. H. & Harrison, D. J. 1997 Transport, manipulation, and reaction of biological cells on-chip using electrokinetic effects. *Anal. Chem.* **69**, 1564–1568.

Liron, N. & Mochon, S. 1976 Stokes flow for a Stokeslet between 2 parallel flat plates. *J. Engng Maths* **10**, 287–303.

Loewenberg, M. & Hinch, E. J. 1996 Numerical simulation of a concentrated emulsion in shear flow. *J. Fluid Mech.* **321**, 395–419.

Lorentz, H. A. 1896 A general theorem concerning the motion of a viscous fluid and a few consequences derived from it. *Zittingsverslag Koninkl. Akad. van Wetensch. Amsterdam* **5**, 168–175.

Pozrikidis, C. 1992 *Boundary Integral and Singularity Methods For Linearized Viscous Flow.* Cambridge University Press.

Pozrikidis, C. 1994 The motion of particles in the Hele-Shaw cell. *J. Fluid Mech.* **261**, 199–222.

Pozrikidis, C. 2005 Orbiting motion of a freely-suspended spheroid near a plane wall. *J. Fluid Mech.* (in press).

Romero, C., Agarwala, J. P. & Davis, R. H. 1993 Separation and classification of axisymmetrical particles in an inclined settler. *Intl J. Multiphase Flow* **19**, 803–816.

Smart, J. R., Beimfohr, S. & Leighton, D. T. 1993 Measurement of the translational and rotational velocities of a noncolloidal sphere rolling down a smooth inclined plane at low Reynolds number. *Phys. Fluids* A **5**, 13–24.

Staben, M. E., Zinchenko, A. Z. & Davis, R. H. 2003 Motion of a particle between two parallel plane walls in low-Reynolds-number Poiseuille flow. *Phys. Fluids* **15**, 1711–1733. *Erratum: Phys. Fluids* **16**, 4206.

Sugihara-Seki, M. 1993 The motion of an elliptic cylinder in channel flow at low Reynolds numbers. *J. Fluid Mech.* **257**, 575–596.

Sugihara-Seki, M. 1996 The motion of an ellipsoid in tube flow at low Reynolds numbers. *J. Fluid Mech.* **324**, 287–308.

Yu, Z. 1993 The creeping motion of a body between two parallel planes with application to osmosis in biological membranes. PhD Dissertation, City University of New York.

Zhao, Y., Galvin, K. P. & Davis, R. H. 2002 Motion of a sphere down a rough plane in a viscous fluid. *Intl J. Multiphase Flow* **28**, 1787–1800.

Zinchenko, A. Z., Rother, M. A. & Davis, R. H. 1997 A novel boundary-integral algorithm for viscous interaction of deformable drops. *Phys. Fluids* **9,** 1493–1511.

Zinchenko, A. Z., Rother, M. A. & Davis, R. H. 1999 Cusping, capture, and breakup of interacting drops by a curvatureless boundary-integral algorithm. *J. Fluid Mech.* **391**, 249–292.